

Efficient and accurate extraction of *in vivo* calcium signals from microendoscopic video data

Pengcheng Zhou^{1,2}, Shanna L. Resendez^{3†}, Jose Rodriguez-Romaguera^{3†}, Jessica C. Jimenez^{4,5†}, Shay Q. Neufeld^{6†}, Andrea Giovannucci⁷, Johannes Friedrich⁷, Eftychios A. Pnevmatikakis⁷, Garret D. Stuber^{3, 8}, Rene Hen^{4,5}, Mazen A. Kheirbek⁹, Bernardo L. Sabatini⁶, Robert E. Kass^{1,10}, Liam Paninski²

*For correspondence:

pz2230@columbia.edu (PZ);
liam@stat.columbia.edu (LP)

[†]These authors contributed equally to this work

Center for the Neural Basis of Cognition and Machine Learning Department, Carnegie Mellon University, Pittsburgh, United States of America; ²Departments of Statistics and Neuroscience, Grossman Center for the Statistics of Mind, Center for Theoretical Neuroscience, Kavli Institute for Brain Science, and NeuroTechnology Center, Columbia University, New York, United States of America; ³Department of Psychiatry, University of North Carolina at Chapel Hill, Chapel Hill, United States of America; ⁴Departments of Neuroscience & Psychiatry, Columbia University, New York, United States of America; ⁵Division of Integrative Neuroscience, Department of Psychiatry, New York State Psychiatric Institute, New York, United States of America; ⁶Howard Hughes Medical Institute, Department of Neurobiology, Harvard Medical School, Boston, United States of America; ⁷Center for Computational Biology, Flatiron Institute, Simons Foundation, New York, United States of America; ⁸Neuroscience Center, Department of Cell Biology and Physiology, University of North Carolina at Chapel Hill, Chapel Hill, United States of America; ⁹Neuroscience Graduate Program, Weill Institute for Neurosciences, Kavli Institute for Fundamental Neuroscience, Department of Psychiatry, University of California, San Francisco, United States of America; ¹⁰Department of Statistics, Carnegie Mellon University, Pittsburgh, United States of America

Abstract *In vivo* calcium imaging through microendoscopic lenses enables imaging of previously inaccessible neuronal populations deep within the brains of freely moving animals. However, it is computationally challenging to extract single-neuronal activity from microendoscopic data, because of the very large background fluctuations and high spatial overlaps intrinsic to this recording modality. Here, we describe a new constrained matrix factorization approach to accurately separate the background and then demix and denoise the neuronal signals of interest. We compared the proposed method against previous independent components analysis and constrained nonnegative matrix factorization approaches. On both simulated and experimental data recorded from mice, our method substantially improved the quality of extracted cellular signals and detected more well-isolated neural signals, especially in noisy data regimes. These advances can in turn significantly enhance the statistical power of downstream analyses, and ultimately improve scientific conclusions derived from microendoscopic data.

39 **Introduction**

40 Monitoring the activity of large-scale neuronal ensembles during complex behavioral states is
 41 fundamental to neuroscience research. Continued advances in optical imaging technology are
 42 greatly expanding the size and depth of neuronal populations that can be visualized. Specifically,
 43 *in vivo* calcium imaging through microendoscopic lenses and the development of miniaturized
 44 microscopes have enabled deep brain imaging of previously inaccessible neuronal populations of
 45 freely moving mice (*Flusberg et al., 2008; Ghosh et al., 2011; Ziv and Ghosh, 2015*). This technique
 46 has been widely used to study the neural circuits in cortical, subcortical, and deep brain areas, such
 47 as hippocampus (*Cai et al., 2016; Rubin et al., 2015; Ziv et al., 2013*), entorhinal cortex (*Kitamura*
 48 *et al., 2015; Sun et al., 2015*), hypothalamus (*Jennings et al., 2015*), prefrontal cortex (PFC) (*Pinto*
 49 *and Dan, 2015*), premotor cortex (*Markowitz et al., 2015*), dorsal pons (*Cox et al., 2016*), basal
 50 forebrain (*Harrison et al., 2016*), striatum (*Barbera et al., 2016; Carvalho Poyraz et al., 2016; Klaus*
 51 *et al., 2017*), amygdala (*Yu et al., 2017*), and other brain regions.

52 Although microendoscopy has potential applications across numerous neuroscience fields (*Ziv*
 53 *and Ghosh, 2015*), methods for extracting cellular signals from this data are currently limited and
 54 suboptimal. Most existing methods are specialized for 2-photon or light-sheet microscopy. However,
 55 these methods are not suitable for analyzing single-photon microendoscopic data because of its
 56 distinct features: specifically, this data typically displays large, blurry background fluctuations due
 57 to fluorescence contributions from neurons outside the focal plane. In Figure 1 we use a typical
 58 microendoscopic dataset to illustrate these effects (see [S1 Video](#) for raw video). Figure 1A shows an
 59 example frame of the selected data, which contains large signals additional to the neurons visible
 60 in the focal plane. These extra fluorescence signals contribute as background that contaminates
 61 the single-neuronal signals of interest. In turn, standard methods based on local correlations for
 62 visualizing cell outlines (*Smith and Häusser, 2010*) are not effective here, because the correlations
 63 in the fluorescence of nearby pixels are dominated by background signals (Figure 1B). For some
 64 neurons with strong visible signals, we can manually draw regions-of-interest (ROI) (Figure 1C).
 65 Following (*Barbera et al., 2016; Pinto and Dan, 2015*), we used the mean fluorescence trace of the
 66 surrounding pixels (blue, Figure 1D) to roughly estimate this background fluctuation; subtracting
 67 it from the raw trace in the neuron ROI yields a relatively good estimation of neuron signal (red,
 68 Figure 1D). Figure 1D shows that the background (blue) has much larger variance than the relatively
 69 sparse neural signal (red); moreover, the background signal fluctuates on similar timescales as the
 70 single-neuronal signal, so we can not simply temporally filter the background away after extraction
 71 of the mean signal within the ROI. This large background signal is likely due to a combination of
 72 local fluctuations resulting from out-of-focus fluorescence or neuropil activity, hemodynamics of
 73 blood vessels, and global fluctuations shared more broadly across the field of view (photo-bleaching
 74 effects, drifts in *z* of the focal plane, etc.), as illustrated schematically in Figure 1E.

75 The existing methods for extracting individual neural activity from microendoscopic data can
 76 be divided into two classes: semi-manual ROI analysis (*Barbera et al., 2016; Klaus et al., 2017;*
 77 *Pinto and Dan, 2015*) and PCA/ICA analysis (*Mukamel et al., 2009*). Unfortunately, both approaches
 78 have well-known flaws (*Resendez et al., 2016*). For example, ROI analysis does not effectively
 79 demix signals of spatially overlapping neurons, and drawing ROIs is laborious for large population
 80 recordings. More importantly, in many cases the background contaminations are not adequately
 81 corrected, and thus the extracted signals are not sufficiently clean enough for downstream analyses.
 82 As for PCA/ICA analysis, it is a linear demixing method and therefore typically fails when the neural
 83 components exhibit strong spatial overlaps (*Pnevmatikakis et al., 2016*), as is the case in the
 84 microendoscopic setting.

85 Recently, constrained nonnegative matrix factorization (CNMF) approaches were proposed
 86 to simultaneously denoise, deconvolve, and demix calcium imaging data (*Pnevmatikakis et al.,*
 87 *2016*). However, current implementations of the CNMF approach were optimized for 2-photon
 88 and light-sheet microscopy, where the background has a simpler spatiotemporal structure. When

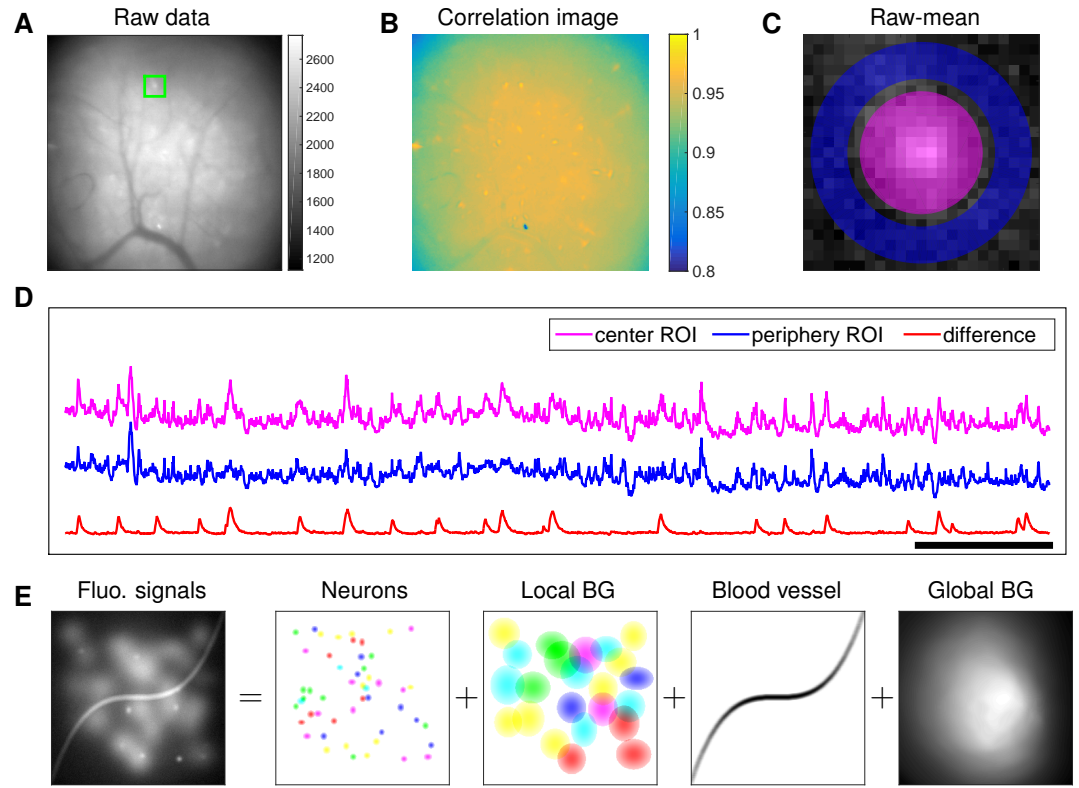


Figure 1. Microendoscopic data contain large background signals with rapid fluctuations due to multiple sources. **(A)** An example frame of microendoscopic data recorded in dorsal striatum (see Methods and Materials section for experimental details). **(B)** The local “correlation image” (Smith and Häusser, 2010) computed from the raw video data. Note that it is difficult to discern neuronal shapes in this image due to the high background spatial correlation level. **(C)** The mean-subtracted data within the cropped area (green) in **(A)**. Two ROIs were selected and coded with different colors. **(D)** The mean fluorescence traces of pixels within the two selected ROIs (magenta and blue) shown in **(C)** and the difference between the two traces. **(E)** Cartoon illustration of various sources of fluorescence signals in microendoscopic data. “BG” abbreviates “background.”

89 applied to microendoscopic data, CNMF often has poor performance because the background is
90 not modeled sufficiently accurately (Barbera et al., 2016).

91 In this paper, we significantly extend the CNMF framework to obtain a robust approach for
92 extracting single-neuronal signals from microendoscopic data. Specifically, our extended CNMF
93 for microendoscopic data (CNMF-E) approach utilizes a more accurate and flexible spatiotemporal
94 background model that is able to handle the properties of the strong background signal illustrated
95 in Fig. 1, along with new specialized algorithms to initialize and fit the model components. After a
96 brief description of the model and algorithms, we first use simulated data to illustrate the power
97 of the new approach. Next, we compare CNMF-E with PCA/ICA analysis comprehensively on both
98 simulated data and four experimental datasets recorded in different brain areas. The results show
99 that CNMF-E outperforms PCA/ICA in terms of detecting more well-isolated neural signals, extracting
100 higher signal-to-noise ratio (SNR) cellular signals, and obtaining more robust results in low SNR
101 regimes. Finally, we show that downstream analyses of calcium imaging data can substantially
102 benefit from these improvements.

Name	Description	Domain
d	number of pixels	\mathbb{N}_+
T	number of frames	\mathbb{N}_+
K	number of neurons	\mathbb{N}
Y	motion corrected video data	$\mathbb{R}_+^{d \times T}$
A	spatial footprints of all neurons	$\mathbb{R}_+^{d \times K}$
C	temporal activities of all neurons	$\mathbb{R}_+^{K \times T}$
B	background activity	$\mathbb{R}_+^{d \times T}$
E	observation noise	$\mathbb{R}_+^{d \times T}$
W	weight matrix to reconstruct B using neighboring pixels	$\mathbb{R}^{d \times d}$
b_0	constant baseline for all pixels	\mathbb{R}_+^d
x_i	spatial location of the i th pixel	\mathbb{N}^2
σ_i	standard deviation of the noise at pixel x_i	\mathbb{R}_+

Table 1. Variables used in the CNMF-E model and algorithm. \mathbb{R} : real numbers; \mathbb{R}_+ : positive real numbers; \mathbb{N} : natural numbers; \mathbb{N}_+ : positive integers.

103 Model and model fitting

104 CNMF for microendoscope data (CNMF-E)

105 The recorded video data can be represented by a matrix $Y \in \mathbb{R}_+^{d \times T}$, where d is the number of
 106 pixels in the field of view and T is the number of frames observed. In our model each neuron i is
 107 characterized by its spatial “footprint” vector $a_i \in \mathbb{R}_+^d$ characterizing the cell’s shape and location,
 108 and “calcium activity” timeseries $c_i \in \mathbb{R}_+^T$, modeling (up to a multiplicative and additive constant) cell
 109 i ’s mean fluorescence signal at each frame. Here, both a_i and c_i are constrained to be nonnegative
 110 because of their physical interpretations. The background fluctuation is represented by a matrix
 111 $B \in \mathbb{R}_+^{d \times T}$. If the field of view contains a total number of K neurons, then the observed movie data
 112 is modeled as a superposition of all neurons’ spatiotemporal activity, plus time-varying background
 113 and additive noise:

$$Y = \sum_{i=1}^K a_i \cdot c_i^T + B + E = AC + B + E, \quad (1)$$

114 where $A = [a_1, \dots, a_K]$ and $C = [c_1, \dots, c_K]^T$. The noise term $E \in \mathbb{R}^{d \times T}$ is modeled as Gaussian, $E(t) \sim$
 115 $\mathcal{N}(\mathbf{0}, \Sigma)$. Σ is a diagonal matrix, indicating that the noise is spatially and temporally uncorrelated.

116 Estimating the model parameters A, C in model (1) gives us all neurons’ spatial footprints and
 117 their denoised temporal activity. This can be achieved by minimizing the residual sum of squares
 118 (RSS), aka the Frobenius norm of the matrix $Y - (AC + B)$,

$$\|Y - (AC + B)\|_F^2, \quad (2)$$

119 while requiring the model variables A, C and B to follow the desired constraints, discussed below.

120 Constraints on neuronal spatial footprints A and neural temporal traces C

121 Each spatial footprint a_i should be spatially localized and sparse, since a given neuron will cover
 122 only a small fraction of the field of view, and therefore most elements of a_i will be zero. Thus we
 123 need to incorporate spatial locality and sparsity constraints on A (*Pnevmatikakis et al., 2016*). We
 124 discuss details further below.

125 Similarly, the temporal components c_i are highly structured, as they represent the cells’ fluo-
 126 rescence responses to sparse, nonnegative trains of action potentials. Following (*Vogelstein et al., 2010*;
 127 *Pnevmatikakis et al., 2016*), we model the calcium dynamics of each neuron c_i with a stable
 128 autoregressive (AR) process of order p ,

$$c_i(t) = \sum_{j=1}^p \gamma_j^{(i)} c_i(t-j) + s_i(t), \quad (3)$$

129 where $s_i(t) \geq 0$ is the number of spikes that neuron fired at the t -th frame. (Note that there is no
 130 further noise input into $c_i(t)$ beyond the spike signal $s_i(t)$.) The AR coefficients $\{\gamma_j^{(i)}\}$ are different
 131 for each neuron and they are estimated from the data. In practice, we usually pick $p = 2$, thus
 132 incorporating both a nonzero rise and decay time of calcium transients in response to a spike; then
 133 Eq. (3) can be expressed in matrix form as

$$G_i \cdot c_i = s_i, \text{ with } G_i = \begin{bmatrix} 1 & 0 & 0 & \dots & 0 \\ -\gamma_1^{(i)} & 1 & 0 & \dots & 0 \\ -\gamma_2^{(i)} & -\gamma_1^{(i)} & 1 & \dots & 0 \\ \vdots & \ddots & \ddots & \ddots & \vdots \\ 0 & \dots & -\gamma_2^{(i)} & -\gamma_1^{(i)} & 1 \end{bmatrix}. \quad (4)$$

134 The neural activity s_i is nonnegative and typically sparse; to enforce sparsity we can penalize the
 135 ℓ_0 (**Jewell and Witten, 2017**) or ℓ_1 (**Pnevmatikakis et al., 2016; Vogelstein et al., 2010**) norm of s_i ,
 136 or limit the minimum size of nonzero spike counts (**Friedrich et al., 2017b**). When the rise time
 137 constant is small compared to the timebin width (low imaging frame rate), we typically use a simpler
 138 AR(1) model (with an instantaneous rise following a spike) (**Pnevmatikakis et al., 2016**).

139 Constraints on background activity B

140 In the above we have largely followed previously-described CNMF approaches (**Pnevmatikakis**
 141 **et al., 2016**) for modeling calcium imaging signals. However, to accurately model the background
 142 effects in microendoscopic data we need to depart significantly from these previous approaches.
 143 Constraints on the background term B in Eq. (1) are essential to the success of CNMF-E, since
 144 clearly, if B is completely unconstrained we could just absorb the observed data Y entirely into
 145 B , which would lead to recovery of no neural activity. At the same time, we need to prevent
 146 the residual of the background term (i.e., $B - \hat{B}$, where \hat{B} denotes the estimated spatiotemporal
 147 background) from corrupting the estimated neural signals AC in model (1), since subsequently,
 148 the extracted neuronal activity would be mixed with background fluctuations, leading to artificially
 149 high correlations between nearby cells. This problem is even worse in the microendoscopic context
 150 because the background fluctuation usually has significantly larger variance than the isolated
 151 cellular signals of interest (Figure 1D), and therefore any small errors in the estimation of B can
 152 severely corrupt the estimated neural signal AC .

153 In (**Pnevmatikakis et al., 2016**), B is modeled as a rank-1 nonnegative matrix $B = b \cdot f^T$, where
 154 $b \in \mathbb{R}_+^d$ and $f \in \mathbb{R}_+^T$. This model mainly captures the global fluctuations within the field of view
 155 (FOV). In applications to 2-photon or light-sheet data, this rank-1 model has been shown to be
 156 sufficient for relatively small spatial regions; the simple low-rank model does not hold for larger
 157 fields of view, and so we can simply divide large FOVs into smaller patches for largely-parallel
 158 processing (**Pnevmatikakis et al., 2016; Giovannucci et al., 2017b**). (See (**Pachitariu et al., 2016**)
 159 for an alternative approach.) However, as we will see below, the local rank-1 model fails in many
 160 microendoscopic datasets, where multiple large overlapping background sources exist even within
 161 modestly-sized FOVs.

162 Thus we propose a new model to constrain the background term B . We first decompose the
 163 background into two terms:

$$B = B^f + B^c, \quad (5)$$

164 where B^f represents fluctuating activity and $B^c = b_0 \cdot \mathbf{1}^T$ models constant baselines ($\mathbf{1} \in \mathbb{R}^T$ denotes
 165 a vector of T ones). To model B^f , we exploit the fact that background sources (largely due to blurred
 166 out-of-focus fluorescence) are empirically much coarser spatially than the average neuron soma
 167 size l . Thus we model B^f at one pixel as a linear combination of the background fluorescence in
 168 pixels which are chosen to be nearby but not nearest neighbors:

$$B_{it}^f = \sum_{j \in \Omega_i} w_{ij} \cdot B_{jt}^f, \quad \forall t = 1 \dots T, \quad (6)$$

169 where $\Omega_i = \{j \mid \text{dist}(\mathbf{x}_i, \mathbf{x}_j) \in [l_n, l_n + 1]\}$, with $\text{dist}(\mathbf{x}_i, \mathbf{x}_j)$ the Euclidean distance between pixel i and j .
 170 Thus Ω_i only selects the neighboring pixels with a distance of l_n from the i -th pixel (the green dot
 171 and black pixels in Figure 2B illustrate i and Ω_i , respectively); here l_n is a parameter that we choose
 172 to be greater than l (the size of the typical soma in the FOV), e.g., $l_n = 2l$. This choice of l_n ensures
 173 that pixels i and j in (6) share similar background fluctuations, but do not belong to the same soma.

174 We can rewrite Eq. (6) in matrix form:

$$\mathbf{B}^f = \mathbf{W} \mathbf{B}^f, \quad (7)$$

175 where $W_{ij} = 0$ if $\text{dist}(\mathbf{x}_i, \mathbf{x}_j) \notin [l_n, l_n + 1]$. In practice, this hard constraint is difficult to enforce
 176 computationally, and is overly stringent given the noisy observed data. We relax the model by
 177 replacing the right-hand side \mathbf{B}^f with the more convenient closed-form expression

$$\mathbf{B}^f = \mathbf{W} \cdot (\mathbf{Y} - \mathbf{AC} - \mathbf{b}_0 \cdot \mathbf{1}^T). \quad (8)$$

178 According to Eq. (1) and (5), this change ignores the noise term E ; since elements in E are spatially
 179 uncorrelated, $\mathbf{W} \cdot E$ contributes as a very small disturbance to $\hat{\mathbf{B}}^f$ in the left-hand side. We found
 180 this substitution for $\hat{\mathbf{B}}^f$ led to significantly faster and more robust model fitting.

181 Fitting the CNMF-E model

Now we can formulate the estimation of all model variables as a single optimization meta-problem:

$$\begin{aligned} & \underset{A, C, S, B^f, W, b_0}{\text{minimize}} && \| \mathbf{Y} - \mathbf{AC} - \mathbf{b}_0 \cdot \mathbf{1}^T - \mathbf{B}^f \|_F^2 \\ & \text{subject to} && A \geq 0, \text{ } A \text{ is sparse and spatially localized} \\ & && c_i \geq 0, s_i \geq 0, G^{(i)}c_i = s_i, s_i \text{ is sparse } \forall i = 1 \dots K \\ & && \mathbf{B}^f \cdot \mathbf{1} = \mathbf{0} \\ & && \mathbf{B}^f = \mathbf{W} \cdot (\mathbf{Y} - \mathbf{AC} - \mathbf{b}_0 \cdot \mathbf{1}^T) \\ & && W_{ij} = 0 \text{ if } \text{dist}(\mathbf{x}_i, \mathbf{x}_j) \notin [l_n, l_n + 1]. \end{aligned} \quad (\text{P-All})$$

182 We call this a “meta-problem” because we have not yet explicitly defined the sparsity and spatial
 183 locality constraints on A and $S = [s_1, \dots, s_K]^T$; these can be customized by users under different
 184 assumptions (see details in Methods and Materials). Also note that s_i is completely determined
 185 by c_i and $G^{(i)}$, and B^f is not optimized explicitly but (as discussed above) can be estimated as
 186 $W \cdot (\mathbf{Y} - \mathbf{AC} - \mathbf{b}_0 \cdot \mathbf{1}^T)$, so we optimize with respect to W instead.

187 The problem (P-All) optimizes all variables together and is non-convex, but can be divided into
 188 three simpler subproblems that we solve iteratively:

Estimating A, b_0 given \hat{C}, \hat{B}^f

$$\begin{aligned} & \underset{A, b_0}{\text{minimize}} && \| \mathbf{Y} - A \cdot \hat{C} - \mathbf{b}_0 \cdot \mathbf{1}^T - \hat{B}^f \|_F^2 \\ & \text{subject to} && A \geq 0, \text{ } A \text{ is sparse and spatially localized} \end{aligned} \quad (\text{P-S})$$

Estimating C, b_0 given \hat{A}, \hat{B}^f

$$\begin{aligned} & \underset{C, S, b_0}{\text{minimize}} && \| \mathbf{Y} - \hat{A} \cdot C - \mathbf{b}_0 \cdot \mathbf{1}^T - \hat{B}^f \|_F^2 \\ & \text{subject to} && c_i \geq 0, s_i \geq 0 \\ & && G^{(i)}c_i = s_i, s_i \text{ is sparse } \forall i = 1 \dots K \end{aligned} \quad (\text{P-T})$$

Estimating W, b_0 given \hat{A}, \hat{C}

$$\begin{aligned} & \underset{W, B^f, b_0}{\text{minimize}} && \| \mathbf{Y} - \hat{A} \cdot \hat{C} - \mathbf{b}_0 \cdot \mathbf{1}^T - B^f \|_F^2 \\ & \text{subject to} && B^f \cdot \mathbf{1} = \mathbf{0} \\ & && B^f = \mathbf{W} \cdot (\mathbf{Y} - \hat{A} \cdot \hat{C} - \mathbf{b}_0 \cdot \mathbf{1}^T) \\ & && W_{ij} = 0 \text{ if } \text{dist}(\mathbf{x}_i, \mathbf{x}_j) \notin [l_n, l_n + 1] \end{aligned} \quad (\text{P-B})$$

189 For each of these subproblems, we are able to use well-established algorithms (e.g., solutions
 190 for (P-S) and (P-T) are discussed in (*Friedrich et al., 2017a; Pnevmatikakis et al., 2016*) or slight
 191 modifications thereof. By iteratively solving these three subproblems, we obtain tractable updates
 192 for all model variables in problem (P-All). Furthermore, this strategy gives us the flexibility of
 193 further potential interventions (either automatic or semi-manual) in the optimization procedure,
 194 e.g., incorporating further prior information on neurons' morphology, or merging/splitting/deleting
 195 spatial components and detecting missed neurons from the residuals. These steps can significantly
 196 improve the quality of the model fitting; this is an advantage compared with PCA/ICA, which offers
 197 no easy option for incorporation of stronger prior information or manually-guided improvements
 198 on the estimates.

199 Full details on the algorithms for initializing and then solving these three subproblems are
 200 provided in the Methods and Materials section.

201 Results

202 CNMF-E can reliably estimate large high-rank background fluctuations

203 We first use simulated data to illustrate the background model in CNMF-E and compare its perfor-
 204 mance against the low-rank NMF model used in the basic CNMF approach (*Pnevmatikakis et al.,*
 205 *2016*). We generated the observed fluorescence Y by summing up simulated fluorescent signals of
 206 multiple sources as shown in Figure 1E plus additive Gaussian white noise (Figure 2A).

207 An example pixel (green dot, Figure 2A,B) was selected to illustrate the background model in
 208 CNMF-E (Eq. (6)), which assumes that each pixel's background activity can be reconstructed using its
 209 neighboring pixels' activities. The selected neighbors form a ring and their distances to the center
 210 pixel are larger than a typical neuron size (Figure 2B). Figure 2C shows that the fluorescence traces
 211 of the center pixel and its neighbors are highly correlated due to the shared large background
 212 fluctuations. Here for illustrative purposes we fit the background by solving problem (P-B) directly
 213 while assuming $\hat{A}\hat{C} = 0$. This mistaken assumption should make the background estimation more
 214 challenging (due to true neural components getting absorbed into the background), but nonetheless
 215 in Figure 2 we see that the background fluctuation was well recovered (Figure 2D). Subtracting this
 216 estimated background from the observed fluorescence in the center yields a good visualization
 217 of the cellular signal (Figure 2D). Thus this example shows that we can reconstruct a complicated
 218 background trace while leaving the neural signal uncontaminated.

219 For the example frame in Figure 2A, the true cellular signals are sparse and weak (Figure 2E).
 220 When we subtract the estimated background using CNMF-E from the raw data, we obtain a good
 221 recovery of the true signal (Figure 2D,F). For comparison, we also estimate the background activity
 222 by applying a rank-1 NMF model as used in basic CNMF; the resulting background-subtracted
 223 image is still severely contaminated by the background (Figure 2G). This is easy to understand: the
 224 spatiotemporal background signal in microendoscopic data typically has a rank higher than one,
 225 due to the various signal sources indicated in Figure 1E), and therefore a rank-1 NMF background
 226 model is insufficient.

227 A naive approach would be to simply increase the rank of the NMF background model. Figure
 228 2H demonstrates that this approach is ineffective: higher-rank NMF does yield generally better
 229 reconstruction performance, but with high variability and low reliability (due to randomness in the
 230 initial conditions of NMF). Eventually as the NMF rank increases many single-neuronal signals of
 231 interest are swallowed up in the estimated background signal (data not shown). In contrast, CNMF-E
 232 recovers the background signal more accurately than any of the high-rank NMF models.

233 In real data analysis settings, the rank of NMF is an unknown and the selection of its value is a
 234 nontrivial problem. We simulated data sets with different numbers of local background sources
 235 and use a single parameter setting to run CNMF-E for reconstructing the background over multiple
 236 such simulations. Figure 2I shows that the performance of CNMF-E does not degrade quickly as
 237 we have more background sources, in contrast to rank-1 NMF. Therefore CNMF-E can recover the

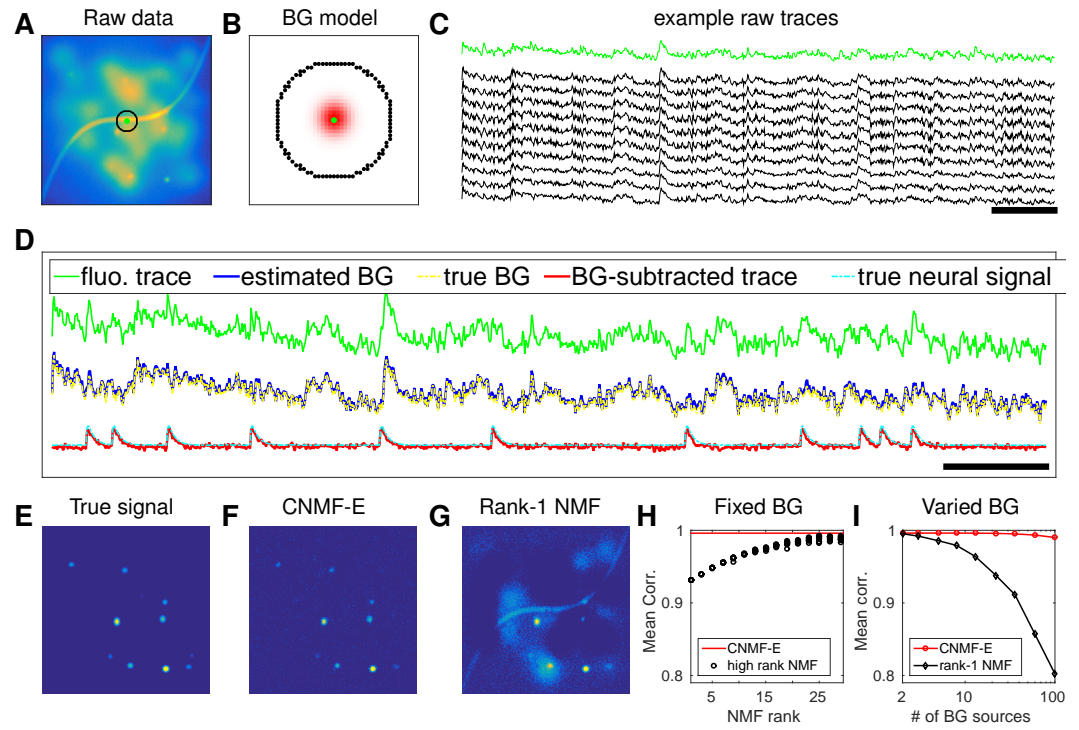


Figure 2. CNMF-E can accurately separate and recover the background fluctuations in simulated data. **(A)** An example frame of simulated microendoscopic data formed by summing up the fluorescent signals from the multiple sources illustrated in Figure 1**E**. **(B)** A zoomed-in version of the circle in **(A)**. The green dot indicates the pixel of interest. The surrounding black pixels are its neighbors with a distance of 15 pixels. The red area approximates the size of a typical neuron in the simulation. **(C)** Raw fluorescence traces of the selected pixel and some of its neighbors on the black ring. Note the high correlation. **(D)** Fluorescence traces (raw data; true and estimated background; true and initial estimate of neural signal) from the center pixel as selected in **(B)**. Note that the background dominates the raw data in this pixel, but nonetheless we can accurately estimate the background and subtract it away here. Scalebars: 10 seconds. Panels **(E–G)** show the cellular signals in the same frame as **(A)**. **(E)** Ground truth neural activity. **(F)** The residual of the raw frame after subtracting the background estimated with CNMF-E; note the close correspondence with **E**. **(G)** Same as **(F)**, but the background is estimated with rank-1 NMF. A video showing **(E–G)** for all frames can be found at [S2 Video](#). **(H)** The mean correlation coefficient (over all pixels) between the true background fluctuations and the estimated background fluctuations. The rank of NMF varies and we run randomly-initialized NMF for 10 times for each rank. The red line is the performance of CNMF-E, which requires no selection of the NMF rank. **(I)** The performance of CNMF-E and rank-1 NMF in recovering the background fluctuations from the data superimposed with an increasing number of background sources.

background accurately across a diverse range of background sources, as desired.

239 CNMF-E accurately initializes single-neuronal spatial and temporal components

240 Next we used simulated data to validate our proposed initialization procedure (Figure 3A). In this
 241 example we simulated 200 neurons with strong spatial overlaps (Figure 3B). One of the first steps in
 242 our initialization procedure is to apply a Gaussian spatial filter to the images to reduce the (spatially
 243 coarser) background and boost the power of neuron-sized objects in the images. In Figure 3C, we
 244 see that the local correlation image ([Smith and Häusser, 2010](#)) computed on the spatially filtered
 245 data provides a good initial visualization of neuron locations; compare to Figure 1B, where the
 246 correlation image computed on the raw data was highly corrupted by background signals.

247 We choose two example ROIs to illustrate how CNMF-E removes the background contamination
 248 and demixes nearby neural signals for accurate initialization of neurons' shapes and activity. In the
 249 first example, we choose a well-isolated neuron (green box, Figure 3A+B). We select three pixels
 250 located in the center, the periphery, and the outside of the neuron and show the corresponding

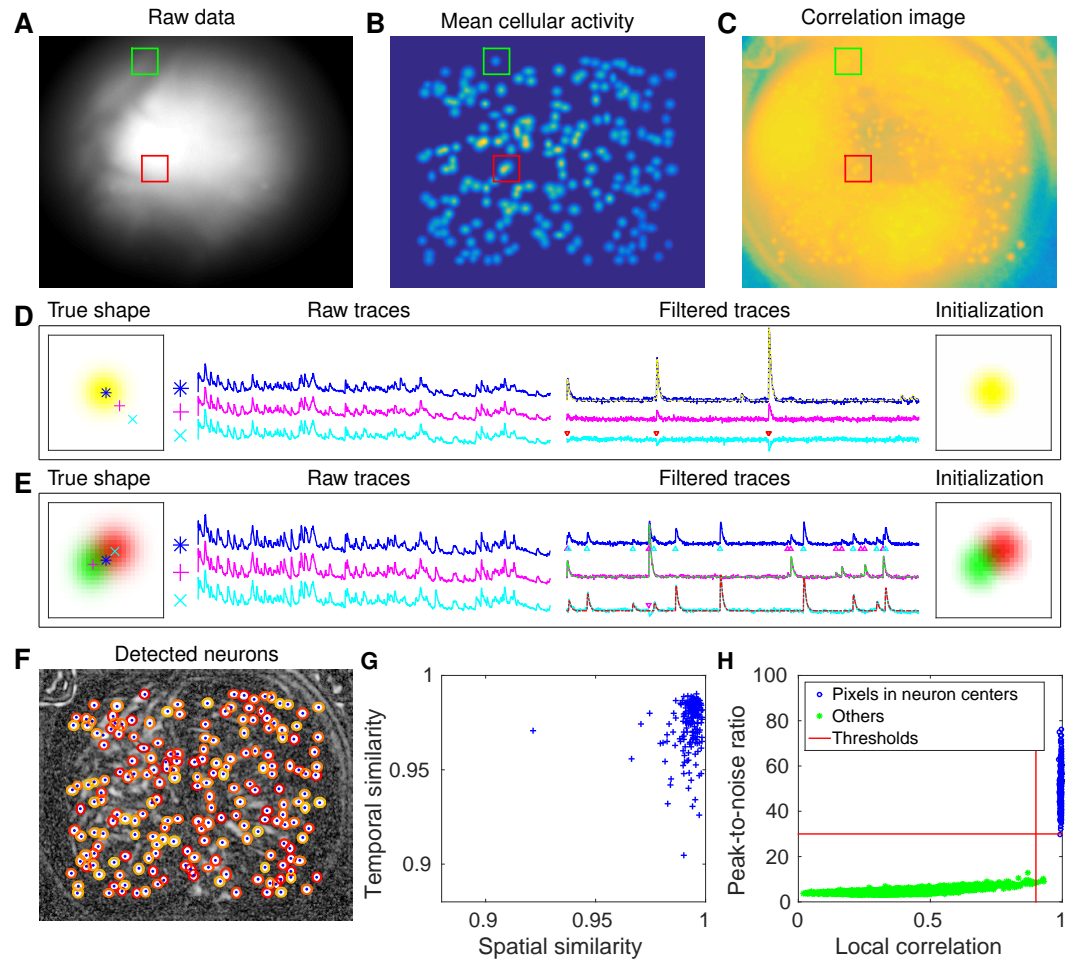


Figure 3. CNMF-E accurately initializes individual neurons' spatial and temporal components in simulated data. **(A)** An example frame of the simulated data. Green and red squares will correspond to panels **(D)** and **(E)** below, respectively. **(B)** The temporal mean of the cellular activity in the simulation. **(C)** The correlation image computed using the spatially filtered data. **(D)** An example of initializing an isolated neuron. Three selected pixels correspond to the center, the periphery, and the outside of a neuron. The raw traces and the filtered traces are shown as well. The yellow dashed line is the true neural signal of the selected neuron. Triangle markers highlight the spike times from the neuron. **(E)** Same as **(D)**, but two neurons are spatially overlapping in this example. Note that in both cases neural activity is clearly visible in the filtered traces, and the initial estimates of the spatial footprints are already quite accurate (dashed lines are ground truth). **(F)** The contours of all initialized neurons on top of the correlation image as shown in **(D)**. Contour colors represent the rank of neurons' SNR (SNR decreases from red to yellow). The blue dots are centers of the true neurons. **(G)** The spatial and the temporal cosine similarities between each simulated neuron and its counterpart in the initialized neurons. **(H)** The local correlation and the peak-to-noise ratio for pixels located in the central area of each neuron (blue) and other areas (green). The red lines are the thresholding boundaries for screening seed pixels in our initialization step. A video showing the whole initialization step can be found at [S3 Video](#).

251 fluorescence traces in both the raw data and the spatially filtered data (Figure 3D). The raw traces
 252 are noisy and highly correlated, but the filtered traces show relatively clean neural signals. This is
 253 because spatial filtering reduces the shared background activity and the remaining neural signals
 254 dominate the filtered data. Similarly, Figure 3E is an example showing how CNMF-E demixes two
 255 overlapping neurons. The filtered traces in the centers of the two neurons still preserve their own
 256 temporal activity.

257 After initializing the neurons' traces using the spatially filtered data, we initialize our estimate of
 258 their spatial footprints. Note that simply initializing these spatial footprints with the spatially-filtered

259 data does not work well (data not shown), since the resulting shapes are distorted by the spatial
 260 filtering process. We found that it was more effective to initialize each spatial footprint by regressing
 261 the initial neuron traces onto the raw movie data (See Methods and Materials for details). The
 262 initial values already match the simulated ground truth with fairly high fidelity (Figure 3D+E). In
 263 this simulated data, CNMF-E successfully identified all 200 neurons and initialized their spatial and
 264 temporal components (Figure 3F). We then evaluate the quality of initialization using all neurons'
 265 spatial and temporal similarities with their counterparts in the ground truth data. Figure 3G shows
 266 that all initialized neurons have high similarities with the truth, indicating a good recovery and
 267 demixing of all neuron sources.

268 Thresholds on the minimum local correlation and the minimum peak-to-noise ratio (PNR) for
 269 detecting seed pixels are necessary for defining the initial spatial components. To quantify the
 270 sensitivity of choosing these two thresholds, we plot the local correlations and the PNRs of all pixels
 271 chosen as the local maxima within an area of $\frac{I}{4} \times \frac{I}{4}$, where I is the diameter of a typical neuron, in
 272 the correlation image or the PNR image (Figure 3H). Pixels are classified into two classes according
 273 to their locations relative to the closest neurons: neurons' central areas and outside areas (see
 274 Methods and Materials for full details). It is clear that the two classes are linearly well separated
 275 and the thresholds can be chosen within a broad range of values (Figure 3H), indicating that the
 276 algorithm is robust with respect to these threshold parameters here. In lower-SNR settings these
 277 boundaries may be less clear, and an incremental approach (in which we choose the highest-SNR
 278 neurons first, then estimate the background and examine the residual to select the lowest-SNR
 279 cells) may be preferred; this incremental approach is discussed in more depth in the Methods and
 280 Materials section.

281 **CNMF-E recovers the true neural activity and is robust to noise contamination and 282 neuronal correlations in simulated data**

283 Using the same simulated dataset as in the previous section, we further refine the neuron shapes
 284 (*A*) and the temporal traces (*C*) by iteratively fitting the CNMF-E model. We compare the final results
 285 with PCA/ICA analysis (*Mukamel et al., 2009*) and the original CNMF method (*Pnevmatikakis et al.,
 286 2016*).

287 After choosing the thresholds for seed pixels (Figure 3H), we run CNMF-E in full automatic mode,
 288 without any manual interventions. Two open-source MATLAB packages, CellSort¹ (*Mukamel, 2016*)
 289 and ca_source_extraction² (*Pnevmatikakis, 2016*), were used to perform PCA/ICA (*Mukamel et al.,
 290 2009*) and basic CNMF (*Pnevmatikakis et al., 2016*), respectively. Since the initialization algorithm
 291 in CNMF fails due to the large contaminations from the background fluctuations in this setting
 292 (recall Figure 2), we use the ground truth as its initialization. As for the rank of the background
 293 model in CNMF, we tried all integer values between 1 and 16 and set it as 7 because it has the best
 294 performance in matching the ground truth. We emphasize that including the CNMF approach in this
 295 comparison is not fair for the other two approaches, because it uses the ground truth heavily, while
 296 PCA/ICA and CNMF-E are blind to the ground truth. The purpose here is to show the limitations of
 297 basic CNMF in modeling the background activity in microendoscopic data.

298 We first pick three closeby neurons from the ground truth (Figure 4A, top) and see how well
 299 these neurons' activities are recovered. PCA/ICA fails to identify one neuron, and for the other
 300 two identified neurons, it recovers temporal traces that are sufficiently noisy that small calcium
 301 transients are submerged in the noise. As for CNMF, the neuron shapes remain more or less at the
 302 initial condition (i.e., the ground truth spatial footprints), but clear contaminations in the temporal
 303 traces are visible. This is because the pure NMF model in CNMF does not model the true background
 304 well and the residuals in the background are mistakenly captured by neural components. In contrast,
 305 on this example, CNMF-E recovers the true neural shapes and neural activity with high accuracy.

¹<https://github.com/mukamel-lab/CellSort>

²https://github.com/epnev/ca_source_extraction

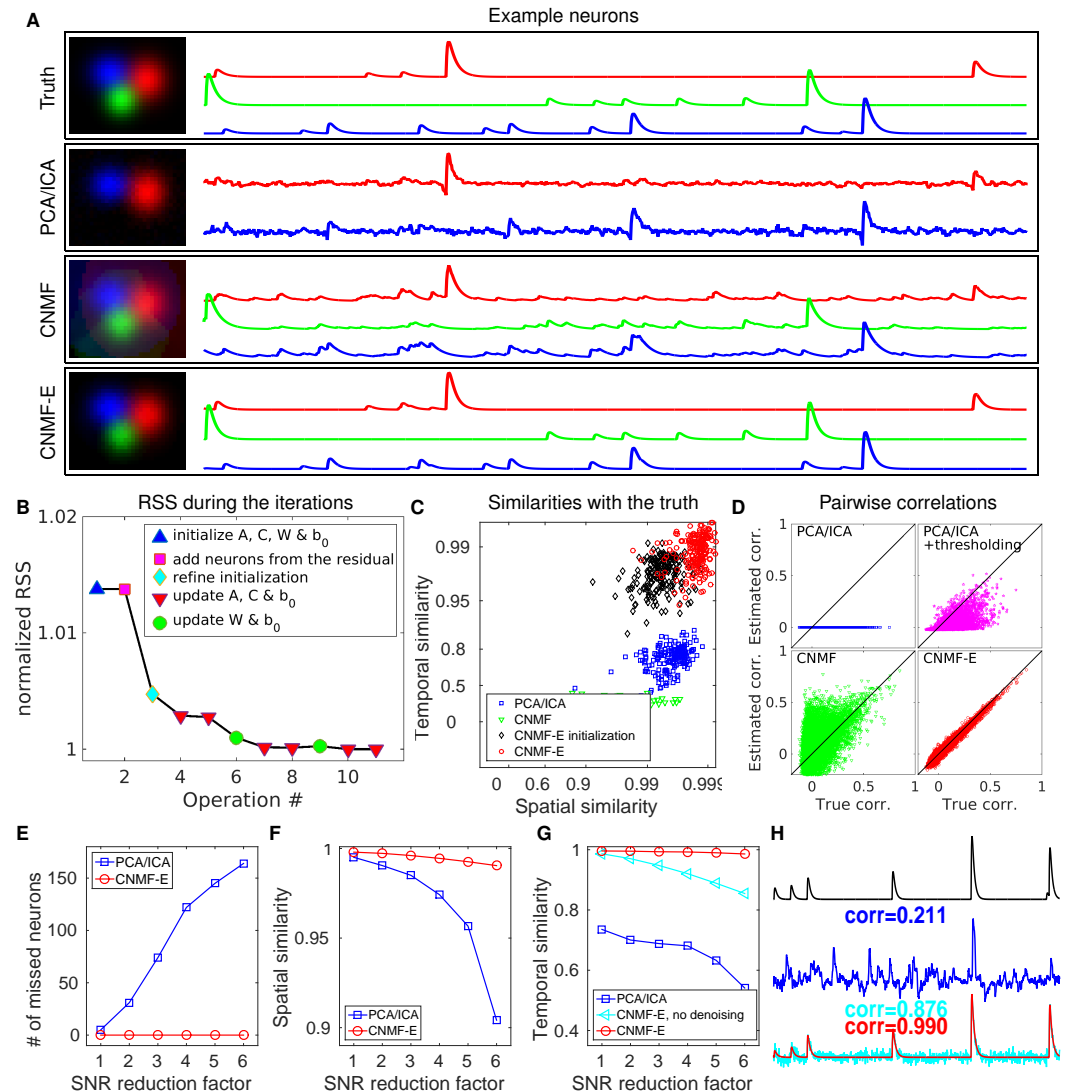


Figure 4. CNMF-E outperforms PCA/ICA analysis in extracting individual neurons' activity from simulated data and is robust to low SNR. **(A)** The results of PCA/ICA, CNMF, and CNMF-E in recovering the spatial footprints and temporal traces of three example neurons. The trace colors match the neuron colors shown in the left. **(B)** The intermediate residual sum of squares (RSS) values (normalized by the final RSS value), during the CNMF-E model fitting. The "refine initialization" step refers to the modification of the initialization results in the case of high temporal correlation (details in Methods and Materials). **(C)** The spatial and the temporal cosine similarities between the ground truth and the neurons detected using different methods. **(D)** The pairwise correlations between the calcium activity traces extracted using different methods. **(E-G)** The performances of PCA/ICA and CNMF-E under different noise levels: the number of missed neurons (**E**), and the spatial (**F**) and temporal (**G**) cosine similarities between the extracted components and the ground truth. **(H)** The calcium traces of one example neuron: the ground truth (black), the PCA/ICA trace (blue), the CNMF-E trace (red) and the CNMF-E trace without being denoised (cyan). The similarity values shown in the figure are computed as the cosine similarity between each trace and the ground truth (black). Two videos showing the demixing results of the simulated data can be found in [S4 Video](#) (SNR reduction factor=1) and [S5 Video](#) (SNR reduction factor=6).

306 We also compare the number of detected neurons: PCA/ICA detected 195 out of 200 neurons,
 307 while CNMF-E detected all 200 neurons. We also quantitatively evaluated the performance of source
 308 extraction by showing the spatial and temporal cosine similarities between detected neurons
 309 and ground truth (Figure 4C); we find that the neurons detected using PCA/ICA have much lower
 310 similarities with the ground truth (Figure 4C). We also note that the CNMF results are much worse

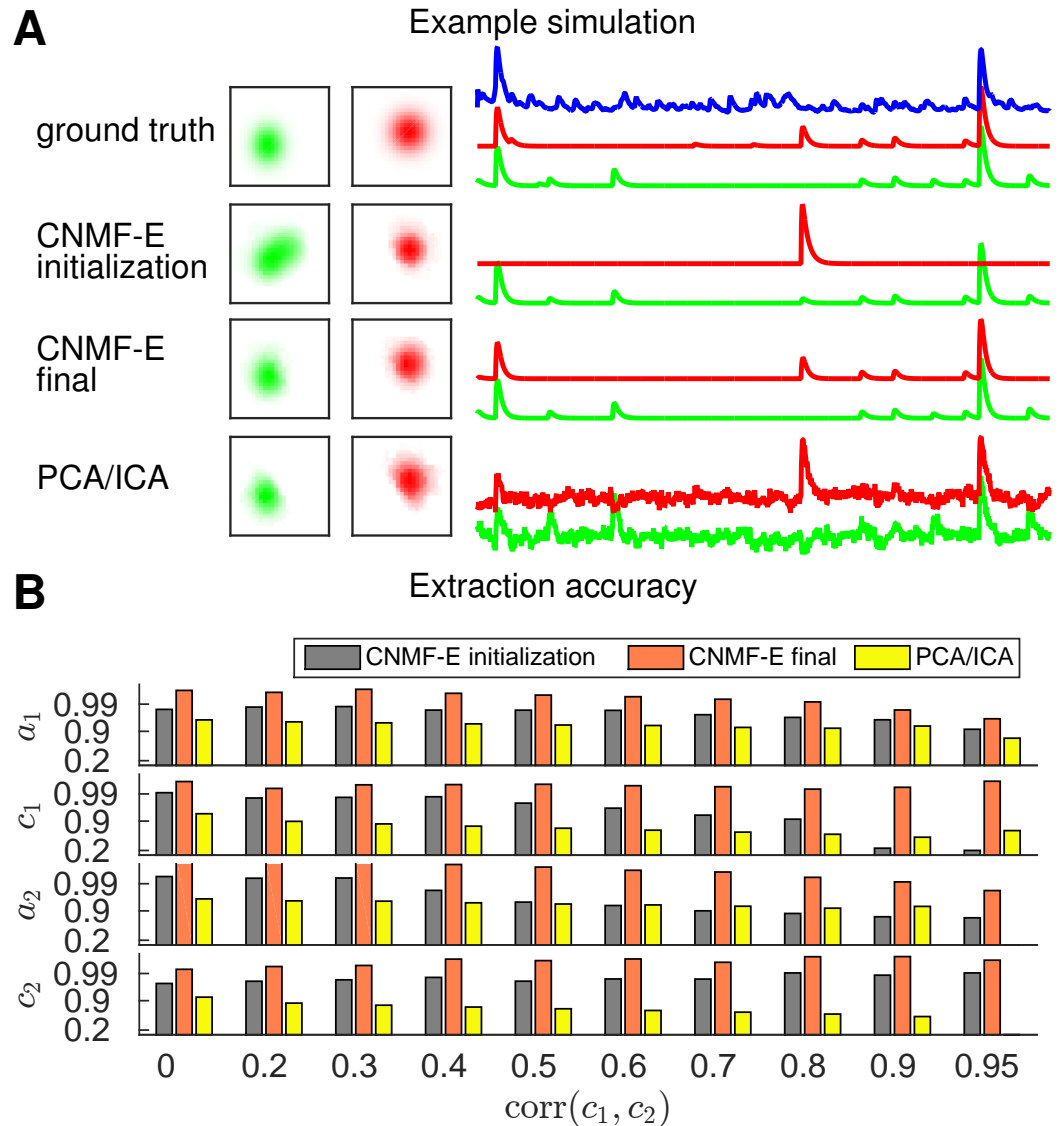


Figure 5. CNMF-E is able to demix neurons with high temporal correlations. **(A)** An example simulation from the experiments summarized in panel **(B)**, where $\text{corr}(c_1, c_2)$ is 0.9: green and red traces correspond to the corresponding neuronal shapes in the left panels. The blue trace is the mean background fluorescence fluctuation over the whole FOV. **(B)** The extraction accuracy of the spatial (a_1 and a_2) and the temporal (c_1 and c_2) components of two close-by neurons, computed via the cosine similarity between the ground truth and the extraction results.

than those of CNMF-E here, despite the fact that CNMF is initialized at the ground truth parameter values. This result clarifies an important point: the improvements from CNMF-E are not simply due to improvements in the initialization step. Furthermore, running the full iterative pipeline of CNMF-E leads to improvements in both spatial and temporal similarities, compared with the results in the initialization step.

In many downstream analyses of calcium imaging data, pairwise correlations provide an important metric to study coordinated network activity (Warp et al., 2012; Barbera et al., 2016; Dombeck et al., 2009; Klaus et al., 2017). Since PCA/ICA seeks statistically independent components, which forces the temporal traces to have near-zero correlation, the correlation structure is badly corrupted in the raw PCA/ICA outputs (Figure 4D). We observed that a large proportion of the independence comes from the noisy baselines in the extracted traces (data not shown), so we postprocessed

322 the PCA/ICA output by thresholding at the 3 standard deviation level. This recovers some nonzero
 323 correlations, but the true correlation structure is not recovered accurately (Figure 4D). By contrast,
 324 the CNMF-E results matched the ground truth very well due to accurate extraction of individual
 325 neurons' temporal activity (Figure 4D). As for CNMF, the estimated correlations are slightly elevated
 326 relative to the true correlations. This is due to the shared (highly correlated) background fluctuations
 327 that corrupt the recovered activity of nearby neurons.

328 Next we compared the performance of the different methods under different SNR regimes.
 329 Because of the above inferior results we skip comparisons to the basic CNMF here. Based on
 330 the same simulation parameters as above, we vary the noise level Σ by multiplying it with a SNR
 331 reduction factor. Figure 4E shows that CNMF-E detects all neurons over a wide SNR range, while
 332 PCA/ICA fails to detect the majority of neurons when the SNR drops to sufficiently low levels.
 333 Moreover, the detected neurons in CNMF-E preserve high spatial and temporal similarities with
 334 the ground truth (Figure 4F-G). This high accuracy of extracting neurons' temporal activity benefits
 335 from the modeling of the calcium dynamics, which leads to significantly denoised neural activity.
 336 If we skip the temporal denoising step in the algorithm, CNMF-E is less robust to noise, but still
 337 outperforms PCA/ICA significantly (Figure 4G). When SNR is low, the improvements yielded by
 338 CNMF-E can be crucial for detecting weak neuron events, as shown in Figure 4H.

339 Finally, we examine the ability of CNMF-E to demix correlated and overlapping neurons. Using
 340 the two example neurons in Figure 3E, we ran multiple simulations at varying correlation levels
 341 and extracted neural components using the CNMF-E pipeline and PCA/ICA analysis. The spatial
 342 footprints in these simulations were fixed, but the temporal components were varied to have
 343 different correlation levels (γ) between calcium traces by tuning their shared component with the
 344 common background fluctuations. For high correlation levels ($\gamma > 0.7$), the initialization procedure
 345 tends to first initialize a component that explains the common activity between two neurons and
 346 then initialize another component to account for the residual of one neuron. After iteratively refining
 347 the model variables, CNMF-E successfully extracted the two neurons' spatiotemporal activity even
 348 at very high correlation levels ($\gamma = 0.95$; Figure 5A,B). PCA/ICA was also often able to separate two
 349 neurons for large correlation levels ($\gamma = 0.9$, Figure 5B), but the extracted traces have problematic
 350 negative spikes that serve to reduce their statistical dependences (Figure 4A).

351 Application to dorsal striatum data

352 We now turn to the analysis of large-scale microendoscopic datasets recorded from freely behaving
 353 mice. We run both CNMF-E and PCA/ICA for all datasets and compare their performances in detail.

354 We begin by analyzing *in vivo* calcium imaging data of neurons expressing GCaMP6f in the
 355 mouse dorsal striatum. (Full experimental details and algorithm parameter settings for this and the
 356 following datasets appear in the Methods and Materials section.) CNMF-E extracted 692 putative
 357 neural components from this dataset; PCA/ICA extracted 547 components (starting from 700 initial
 358 components, and then automatically removing false positives using the same criterion as applied in
 359 CNMF-E). Figure 6A shows how CNMF-E decomposes an example frame into four components: the
 360 constant baselines that are invariant over time, the fluctuating background, the denoised neural
 361 signals, and the residuals. We highlight an example neuron by drawing its ROI to demonstrate the
 362 power of CNMF-E in isolating fluorescence signals of neurons from the background fluctuations.
 363 For the selected neuron, we plot the mean fluorescence trace of the raw data and the estimated
 364 background (Figure 6B). These two traces are very similar, indicating that the background fluctuation
 365 dominates the raw data. By subtracting this estimated background component from the raw data,
 366 we acquire a clean trace that represents the neural signal.

367 To quantify the background effects further, we compute the contribution of each signal compo-
 368 nent in explaining the variance in the raw data. For each pixel, we compute the variance of the raw
 369 data first and then compute the variance of the background-subtracted data. Then the reduced
 370 variance is divided by the variance of the raw data, giving the proportion of variance explained
 371 by the background. Figure 6C (blue) shows the distribution of the background-explained variance

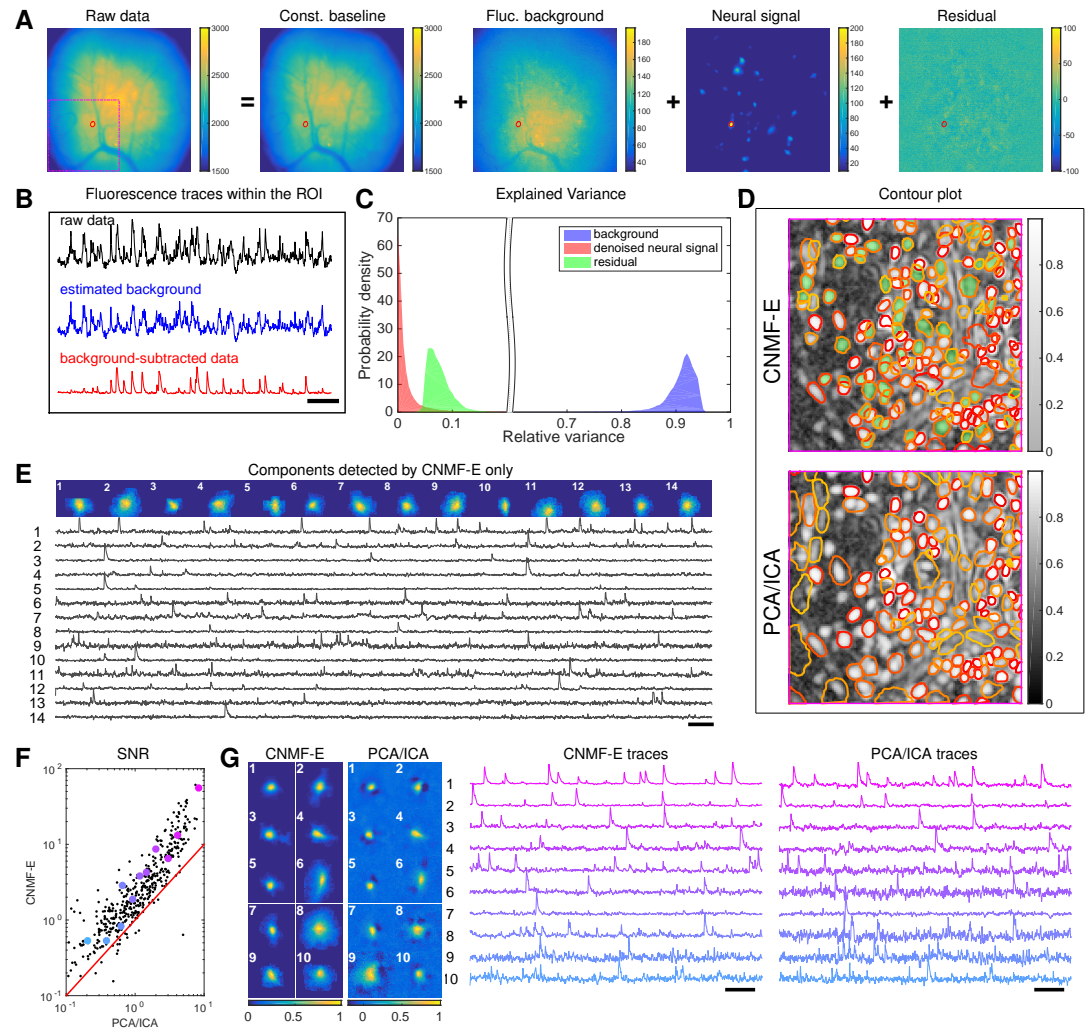


Figure 6. Neurons expressing GCaMP6f recorded *in vivo* in mouse dorsal striatum area. **(A)** An example frame of the raw data and its four components decomposed by CNMF-E. **(B)** The mean fluorescence traces of the raw data (black), the estimated background activity (blue), and the background-subtracted data (red) within the segmented area (red) in **(A)**. The variance of the black trace is about 2x the variance of the blue trace and 4x the variance of the red trace. **(C)** The distributions of the variance explained by different components over all pixels; note that estimated background signals dominate the total variance of the signal. **(D)** The contour plot of all neurons detected by CNMF-E and PCA/ICA superimposed on the correlation image. Green areas represent the components that are only detected by CNMF-E. The components are sorted in decreasing order based on their SNRs (from red to yellow). **(E)** The spatial and temporal components of 14 example neurons that are only detected by CNMF-E. These neurons all correspond to green areas in **(D)**. **(F)** The signal-to-noise ratios (SNRs) of all neurons detected by both methods. Colors match the example traces shown in **(G)**, which shows the spatial and temporal components of 10 example neurons detected by both methods. Scalebar: 10 seconds. See [S6 Video](#) for the demixing results.

372 over all pixels. The background accounts for around 90% of the variance on average. We further
 373 remove the denoised neural signals and compute the variance reduction; Figure 6C shows that
 374 neural signals account for less than 10% of the raw signal variance. This analysis is consistent with
 375 our observations that background dominates the fluorescence signal and extracting high-quality
 376 neural signals requires careful background signal removal.

377 The contours of the spatial footprints inferred by the two approaches (PCA/ICA and CNMF-E)
 378 are depicted in Figure 6D, superimposed on the correlation image of the filtered raw data. The
 379 indicated area was cropped from Figure 6A (left). In this case, most neurons inferred by PCA/ICA

380 were inferred by CNMF-E as well, with the exception of a few components that seemed to be false
 381 positives (judging by their spatial shapes and temporal traces and visual inspection of the raw
 382 data movie; detailed data not shown). However, many realistic components were only detected by
 383 CNMF-E (shown as the green areas in Figure 6D). In these plots, we rank the inferred components
 384 according to their SNRs; the color indicates the relative rank (decaying from red to yellow). We see
 385 that the components missed by PCA/ICA have low SNRs (green shaded areas with yellow contours).

386 Figure 6E shows the spatial and temporal components of 14 example neurons detected only by
 387 CNMF-E. Here (and in the following figures), for illustrative purposes, we show the calcium traces
 388 before the temporal denoising step. For neurons that are inferred by both methods, CNMF-E shows
 389 significant improvements in the SNR of the extracted cellular signals (Figure 6F), even before the
 390 temporal denoising step is applied. In panel G we randomly select 10 examples and examine their
 391 spatial and temporal components. Compared with the CNMF-E results, PCA/ICA components have
 392 much smaller size, often with negative dips surrounding the neuron (remember that ICA avoids
 393 spatial overlaps in order to reduce nearby neurons' statistical dependences, leading to some loss of
 394 signal strength; see (*Pnevmatikakis et al., 2016*) for further discussion). The activity traces extracted
 395 by CNMF-E are visually cleaner than the PCA/ICA traces; this is important for reliable event detection,
 396 particularly in low SNR examples. See (*Klaus et al., 2017*) for additional examples of CNMF-E applied
 397 to striatal data.

398 **Application to data in prefrontal cortex**

399 We repeat a similar analysis on GCaMP6s data recorded from prefrontal cortex (PFC, Figure 7),
 400 to quantify the performance of the algorithm in a different brain area with a different calcium
 401 indicator. Again we find that CNMF-E successfully extracts neural signals from a strong fluctuating
 402 background (Figure 7A), which contributes a large proportion of the variance in the raw data (Figure
 403 7B). Similarly as with the striatum data, PCA/ICA analysis missed many components that have
 404 very weak signals (33 missed components here). For the matched neurons, CNMF-E shows strong
 405 improvements in the SNRs of the extracted traces (Figure 7D). Consistent with our observation in
 406 striatum (Figure 6G), the spatial footprints of PCA/ICA components are shrunk to promote statistical
 407 independence between neurons, while the neurons inferred by CNMF-E have visually reasonable
 408 morphologies (Figure 6E). As for calcium traces with high SNRs (Figure 7E, cell 1 – 6), CNMF-E traces
 409 have smaller noise values, which is important for detecting small calcium transients (Figure 7E, cell
 410 4). For traces with low SNRs (Figure 7, cell 7 – 10), it is challenging to detect any calcium events
 411 from the PCA/ICA traces due to the large noise variance; CNMF-E is able to visually recover many of
 412 these weaker signals. For those cells missed by PCA/ICA, their traces extracted by CNMF-E have
 413 reasonable morphologies and visible calcium events (Figure 7F).

414 The demixing performance of PCA/ICA analysis can be relatively weak because it is inherently a
 415 linear demixing method (*Pnevmatikakis et al., 2016*). Since CNMF-E uses a more suitable nonlinear
 416 matrix factorization method, it has a better capability of demixing spatially overlapping neurons.
 417 As an example, Figure 7G shows three closeby neurons identified by both CNMF-E and PCA/ICA
 418 analysis. PCA/ICA forces its obtained filters to be spatially separated to reduce their dependence
 419 (thus reducing the effective signal strength), while CNMF-E allows inferred spatial components
 420 to have large overlaps (Figure 7G, left), retaining the full signal power. In the traces extracted
 421 by PCA/ICA, the component labeled in green contains many negative "spikes," which are highly
 422 correlated with the spiking activity of the blue neuron (Figure 7G, yellow). In addition, the green
 423 PCA/ICA neuron has significant crosstalk with the red neuron due to the failure of signal demixing
 424 (Figure 7G, cyan); the CNMF-E traces shows no comparable negative "spikes" or crosstalk. See also
 425 [S8 Video](#) for further details.

426 **Application to ventral hippocampus neurons**

427 In the previous two examples, we analyzed data with densely packed neurons, in which the neuron
 428 sizes are all similar. In the next example, we apply CNMF-E to a dataset with much sparser and

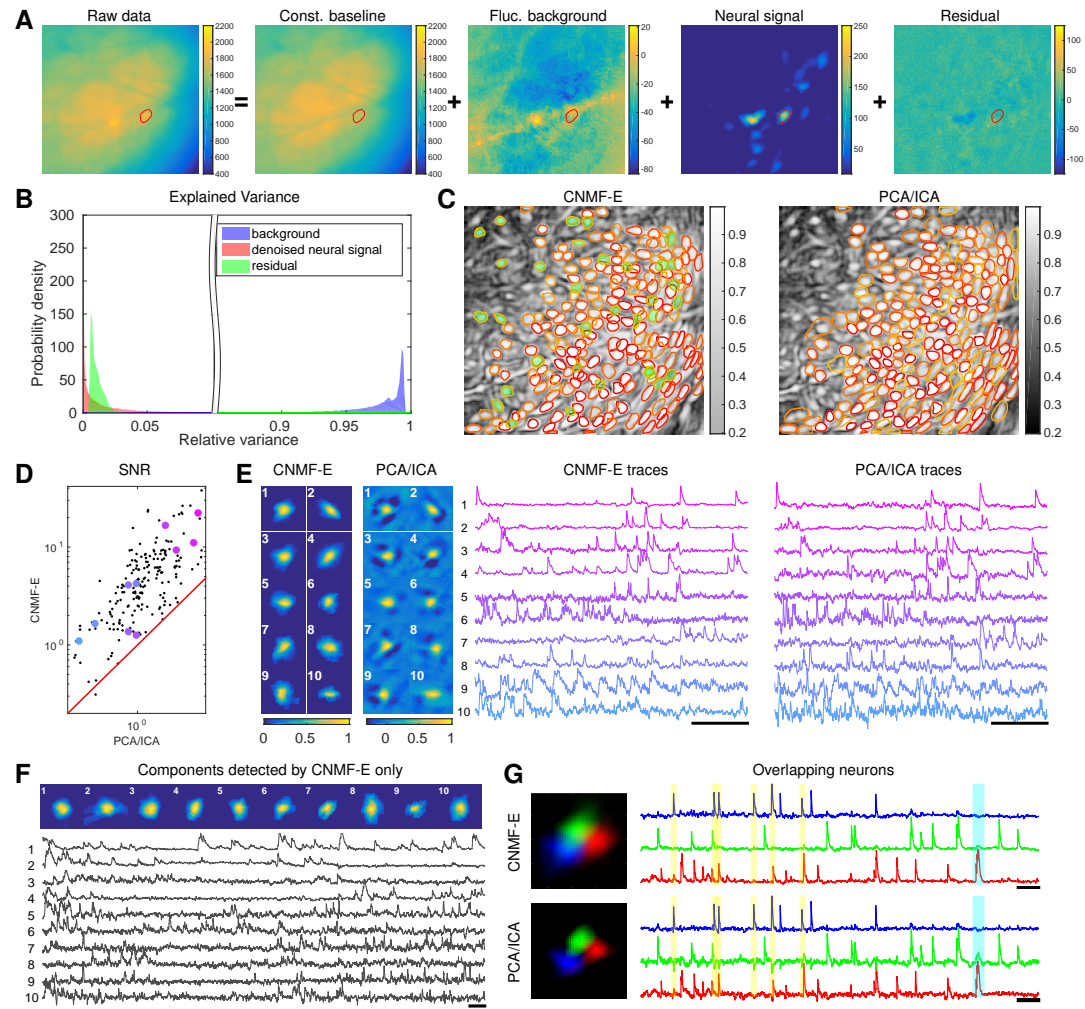


Figure 7. Neurons expressing GCaMP6s recorded *in vivo* in mouse prefrontal cortex. **(A-F)** follow similar conventions as in the corresponding panels of Figure 6. **(G)** Three example neurons that are close to each other and detected by both methods. Yellow shaded areas highlight the negative ‘spikes’ correlated with nearby activity, and the cyan shaded area highlights one crosstalk between nearby neurons. Scalebar: 20 seconds. See [S7 Video](#) for the demixing results and [S8 Video](#) for the comparison of CNMF-E and PCA/ICA in the zoomed-in area of **(G)**.

more heterogeneous neural signals. The data used here were recorded from amygdala-projecting neurons expressing GCaMP6f in ventral hippocampus. In this dataset, some neurons that are slightly above or below the focal plane were visible with prominent signals, though their spatial shapes are larger than neurons in the focal plane.

This example is somewhat more challenging due to the large diversity of neuron sizes. It is possible to set multiple parameters to detect neurons of different sizes (or to e.g. differentially detect somas versus smaller segments of axons or dendrites passing through the focal plane), but for illustrative purposes here we use a single neural size parameter to initialize all of the components. This in turn splits some large neurons into multiple components. Following this crude initialization step, we updated the background component and then picked the missing neurons from the residual using a second greedy component initialization step. Next we ran CNMF-E for three iterations of updating the model variables A , C , and B . The first two iterations were performed automatically; we included manual interventions (e.g., merging/deleting components) before the last iteration, leading to improved source extraction results (see [S10 Video](#) for details

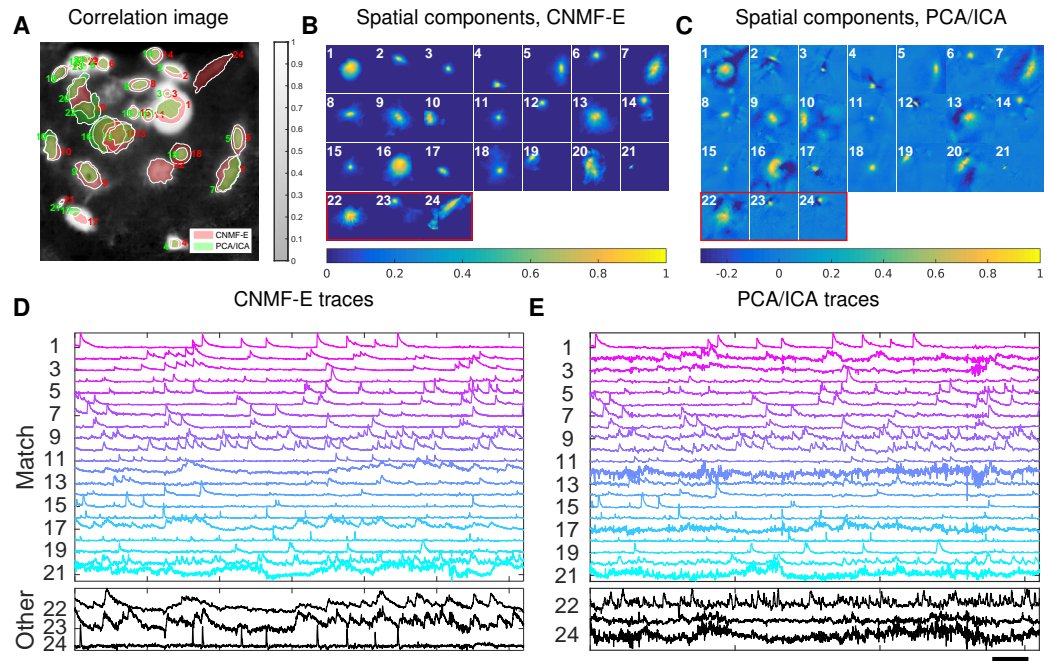


Figure 8. Neurons expressing GCaMP6f recorded *in vivo* in mouse ventral hippocampus. **(A)** Contours of all neurons detected by CNMF-E (red) and PCA/ICA method (green). The grayscale image is the local correlation image of the background-subtracted video data, with background estimated using CNMF-E. **(B)** Spatial components of all neurons detected by CNMF-E. The neurons in the first three rows are also detected by PCA/ICA, while the neurons in the last row are only detected by CNMF-E. **(C)** Spatial components of all neurons detected by PCA/ICA; similar to **(B)**, the neurons in the first three rows are also detected by CNMF-E and the neurons in the last row are only detected by PCA/ICA method. **(D)** Temporal traces of all detected components in **(B)**. ‘Match’ indicates neurons in top three rows in panel **(B)**; ‘Other’ indicates neurons in the fourth row. **(E)** Temporal traces of all components in **(C)**. Scalebars: 20 seconds. See [S9 Video](#) for demixing results.

443 on the manual merge and delete interventions performed here). In this example, we detected 24
 444 CNMF-E components and 24 PCA/ICA components. The contours of these inferred neurons are
 445 shown in Figure 8A. In total we have 20 components detected by both methods (shown in the first
 446 three rows of Figure 8B+C); each method detected extra components that are not detected by the
 447 other (the last rows of Figure 8B+C). Once again, the PCA/ICA filters contain many negative pixels in
 448 an effort to reduce spatial overlaps; see components 3 and 5 in Figure 8A-C, for example. All traces
 449 of the inferred neurons are shown in Figure 8D+E. We can see that the CNMF-E traces have much
 450 lower noise level and cleaner neural signals in both high and low SNR settings. Conversely, the
 451 calcium traces of the 3 extra neurons identified by PCA/ICA show noisy signals that are unlikely to
 452 be neural responses.

453 **Application to footshock responses in the bed nucleus of the stria terminalis (BNST)**
 454 Identifying neurons and extracting their temporal activity is typically just the first step in the analysis
 455 of calcium imaging data; downstream analyses rely heavily on the quality of this initial source
 456 extraction. We showed above that, compared to PCA/ICA, CNMF-E is better at extracting activity
 457 dynamics, especially in regimes where neuronal activities are correlated (c.f. Figure 4D). Using
 458 *in vivo* electrophysiological recordings, we previously showed that neurons in the bed nucleus of
 459 the stria terminalis (BNST) show strong responses to unpredictable footshock stimuli ([Jennings et al., 2013](#)). We therefore measured calcium dynamics in CaMKII-expressing neurons that were
 460 transfected with the calcium indicator GCaMP6s in the BNST and analyzed the synchronous activity
 461 of multiple neurons in response to unpredictable footshock stimuli. We chose 12 example neurons
 462 that were detected by both CNMF-E and PCA/ICA methods and show their spatial and temporal

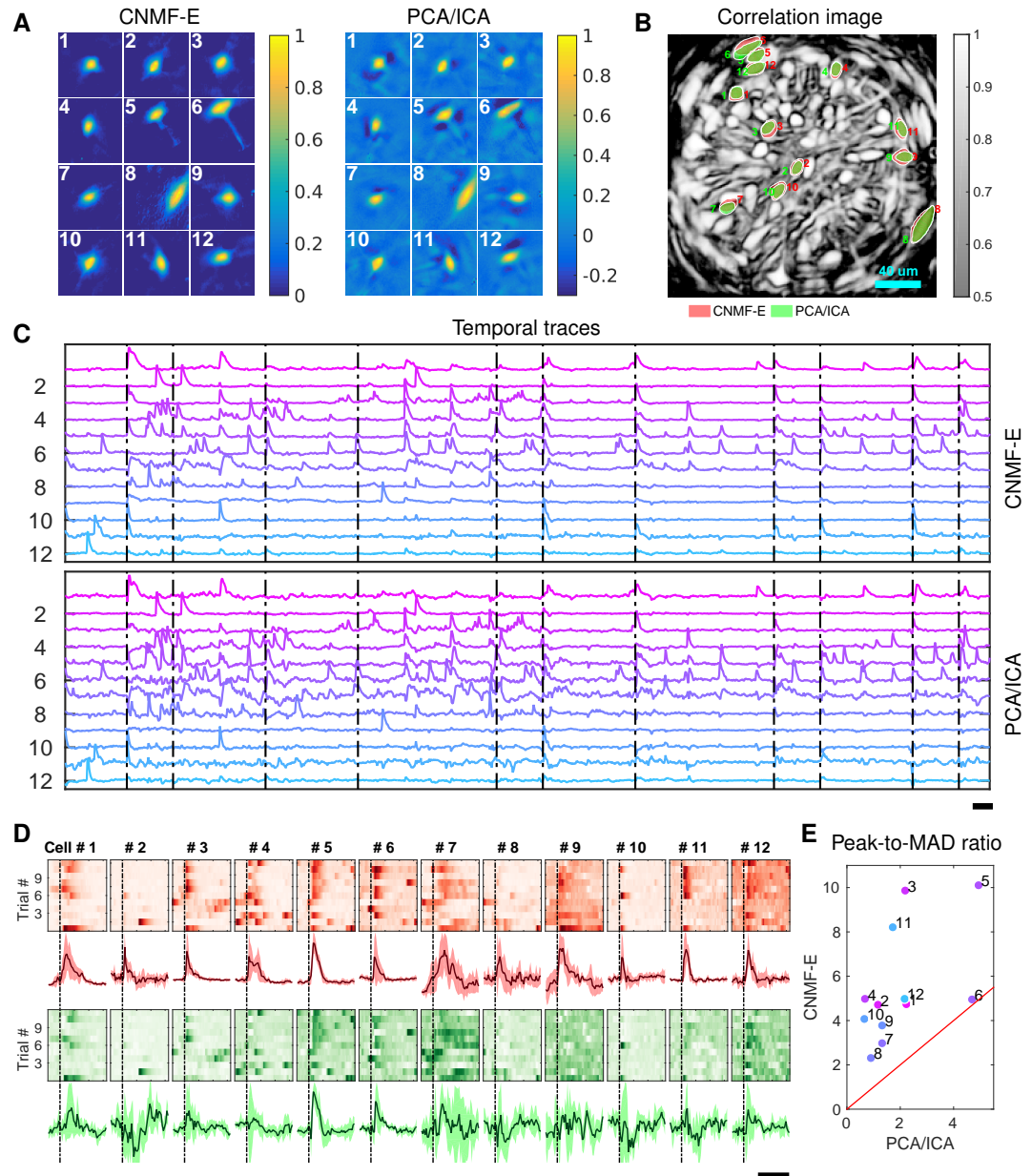


Figure 9. Neurons extracted by CNMF-E show more reproducible responses to footshock stimuli, with larger signal sizes relative to the across-trial variability, compared to PCA/ICA. **(A-C)** Spatial components (**A**), spatial locations (**B**) and temporal components (**C**) of 12 example neurons detected by both CNMF-E and PCA/ICA. **(D)** Calcium responses of all example neurons to footshock stimuli. Colormaps show trial-by-trial responses of each neuron, extracted by CNMF-E (top, red) and PCA/ICA (bottom, green), aligned to the footshock time. The solid lines are medians of neural responses over 11 trials and the shaded areas correspond to median ± 1 median absolute deviation (MAD). Dashed lines indicate the shock timings. **(E)** Scatter plot of peak-to-MAD ratios for all response curves in **(D)**. For each neuron, Peak is corrected by subtracting the mean activity within 4 seconds prior to stimulus onset and MAD is computed as the mean MAD values over all timebins shown in **(D)**. The red line shows $y = x$. Scalebars: 10 seconds. See S11 Video for demixing results.

464 components in Figure 9A-C. The activity around the onset of the repeated stimuli are aligned and
 465 shown as pseudo-colored images in panel D. The median responses of CNMF-E neurons display
 466 prominent responses to the footshock stimuli compared with the resting state before stimuli onset.
 467 In comparison, the activity dynamics extracted by PCA/ICA have relatively low SNR, making it more

468 challenging to reliably extract footshock responses. Panel E summarizes the results of panel D;
 469 we see that CNMF-E outputs significantly more easily detectable responses than does PCA/ICA.
 470 This is an example in which downstream analyses of calcium imaging data can significantly benefit
 471 from the improvements in the accuracy of source extraction offered by CNMF-E. (*Sheintuch et al.*
 472 *(2017)* recently presented another such example, showing that more neurons can be tracked across
 473 multiple days using CNMF-E outputs, compared to PCA/ICA.)

474 Conclusion

475 Microendoscopic calcium imaging offers unique advantages and has quickly become a critical
 476 method for recording large neural populations during unrestrained behavior. However, previous
 477 methods fail to adequately remove background contaminations when demixing single neuron
 478 activity from the raw data. Since strong background signals are largely inescapable in the context of
 479 one-photon imaging, insufficient removal of the background could yield problematic conclusions
 480 in downstream analysis. This has presented a severe and well-known bottleneck in the field. We
 481 have delivered a solution for this critical problem, building on the constrained nonnegative matrix
 482 factorization framework introduced in *Pnevmatikakis et al. (2016)* but significantly extending it in
 483 order to more accurately and robustly remove these contaminating background components.

484 The proposed CNMF-E algorithm can be used in either automatic or semi-automatic mode, and
 485 leads to significant improvements in the accuracy of source extraction compared with previous
 486 methods. In addition, CNMF-E requires very few parameters to be specified, and these parameters
 487 are easily interpretable and can be selected within a broad range. We demonstrated the power
 488 of CNMF-E using data from a wide diversity of brain areas (subcortical, cortical, and deep brain
 489 areas), SNR regimes, calcium indicators, neuron sizes and densities, and hardware setups. Among
 490 all these examples (and many others not shown here), CNMF-E performs well and improves
 491 significantly on the standard PCA/ICA approach. Considering that source extraction is typically
 492 just the first step in calcium imaging data analysis pipelines (*Mohammed et al., 2016*), these
 493 improvements should in turn lead to more stable and interpretable results from downstream
 494 analyses. Further applications of the CNMF-E approach appear in (*Cameron et al., 2016; Donahue*
and Kreitzer, 2017; Jimenez et al., 2016, 2017; Klaus et al., 2017; Lin et al., 2017; Murugan et al.,
2016, 2017; Rodriguez-Romaguera et al., 2017; Tombaz et al., 2016; Ung et al., 2017; Yu et al., 2017;
Mackevicius et al., 2017; Madangopal et al., 2017; Roberts et al., 2017; Ryan et al., 2017; Roberts
et al., 2017; Sheintuch et al., 2017).

499 We have released our MATLAB implementation of CNMF-E as open-source software (https://github.com/zhoupc/CNMF_E) (*Zhou, 2017a*). A Python implementation has also been incorporated
 500 into the CalmAn toolbox (*Giovannucci et al., 2017b*). We welcome additions or suggestions for mod-
 501 ifications of the code, and hope that the large and growing microendoscopic imaging community
 502 finds CNMF-E to be a helpful tool in furthering neuroscience research.

504 Methods and Materials

505 Algorithm for solving problem (P-S)

In problem (P-S), \mathbf{b}_0 is unconstrained and can be updated in closed form: $\hat{\mathbf{b}}_0 = \frac{1}{T}(\tilde{\mathbf{Y}} - \mathbf{A} \cdot \hat{\mathbf{C}} - \hat{\mathbf{B}}^f) \cdot \mathbf{1}$. By plugging this update into problem (P-S), we get a reduced problem

$$\begin{aligned} & \underset{\mathbf{A}}{\text{minimize}} && \|\tilde{\mathbf{Y}} - \mathbf{A} \cdot \tilde{\mathbf{C}}\|_F^2 \\ & \text{subject to} && \mathbf{A} \geq 0, \text{ A is local and sparse}, \end{aligned} \tag{P-S'}$$

where $\tilde{\mathbf{Y}} = \mathbf{Y} - \hat{\mathbf{B}}^f - \frac{1}{T}\mathbf{Y}\mathbf{1}\mathbf{1}^T$ and $\tilde{\mathbf{C}} = \hat{\mathbf{C}} - \frac{1}{T}\hat{\mathbf{C}}\mathbf{1}\mathbf{1}^T$. We approach this problem using a version
 of "hierarchical alternating least squares" (HALS; *Cichocki et al. (2007)*), a standard algorithm for
 nonnegative matrix factorization. (*Friedrich et al. (2017b)* modified the fastHALS algorithm (*Cichocki*
and Phan, 2009) to estimate the nonnegative spatial components \mathbf{A}, \mathbf{b} and the nonnegative temporal

activity C, f in the CNMF model $Y = A \cdot C + b f^T + E$ by including sparsity and localization constraints. We solve a problem similar to the subproblem solved in **Friedrich et al. (2017b)**:

$$\begin{aligned} & \underset{A}{\text{minimize}} && \|\tilde{Y} - A \cdot \tilde{C}\|_F^2 \\ & \text{subject to} && A \geq 0 \\ & && A(i, k) = 0 \forall x_i \notin P_k \end{aligned} \quad (\text{P-S''})$$

where P_k denotes the spatial patch constraining the nonzero pixels of the k -th neuron and restricts the candidate spatial support of neuron k . This regularization reduces the number of free parameters in A , leading to speed and accuracy improvements. The spatial patches can be determined using a mildly dilated version of the support of the previous estimate of A (**Pnevmatikakis et al., 2016; Friedrich et al., 2017a**).

Algorithms for solving problem (P-T)

In problem (P-T), the model variable $C \in \mathbb{R}^{K \times T}$ could be very large, making the direct solution of (P-T) computationally expensive. Unlike problem (P-S), the problem (P-T) cannot be readily parallelized because the constraints $G^{(i)}c_i \geq 0$ couple the entries within each row of C , and the residual term couples entries across columns. Here, we follow the block coordinate-descent approach used in (**Pnevmatikakis et al., 2016**) and propose an algorithm that sequentially updates each c_i and b_0 . For each neuron, we start with a simple unconstrained estimate of c_i , denoted as \hat{y}_i , that minimizes the residual of the spatiotemporal data matrix while fixing other neurons' spatiotemporal activity and the baseline term b_0 ,

$$\hat{y}_i = \underset{c_i \in \mathbb{R}^T}{\text{argmin}} \|Y - \hat{A}_{\setminus i} \cdot \hat{C}_{\setminus i} - \hat{\mathbf{a}}_i c_i - \hat{\mathbf{b}}_0 \cdot \mathbf{1}^T - \hat{B}^f\|_F^2 = \hat{c}_i + \frac{\hat{\mathbf{a}}_i^T \cdot Y_{\text{res}}}{\hat{\mathbf{a}}_i^T \hat{\mathbf{a}}_i}, \quad (9)$$

where $Y_{\text{res}} = Y - \hat{A}\hat{C} - \hat{\mathbf{b}}_0\mathbf{1}^T - \hat{B}^f$ represents the residual given the current estimate of the model variables. Due to its unconstrained nature, \hat{y}_i is a noisy estimate of c_i , plus a constant baseline resulting from inaccurate estimation of b_0 . Given \hat{y}_i , various deconvolution algorithms can be applied to obtain the denoised trace \hat{c}_i and deconvolved signal \hat{s}_i (**Vogelstein et al., 2009; Pnevmatikakis et al., 2013; Deneux et al., 2016; Friedrich et al., 2017b; Jewell and Witten, 2017**); in CNMF-E, we use the OASIS algorithm from (**Friedrich et al., 2017b**). (Note that the estimation of c_i is not dependent on accurate estimation of b_0 , because the algorithm for estimating c_i will also automatically estimate the baseline term in \hat{y}_i .) After the c_i 's are updated, we update b_0 using the closed-form expression $\hat{\mathbf{b}}_0 = \frac{1}{T}(\tilde{Y} - \hat{A} \cdot \hat{C} - \hat{B}^f) \cdot \mathbf{1}$.

Estimating background by solving problem (P-B)

Next we discuss our algorithm for estimating the spatiotemporal background signal by solving problem (P-B) as a linear regression problem given \hat{A} and \hat{C} . Since $B^f \cdot \mathbf{1} = \mathbf{0}$, we can easily estimate the constant baselines for each pixel as

$$\hat{\mathbf{b}}_0 = \frac{1}{T}(Y - \hat{A} \cdot \hat{C}) \cdot \mathbf{1}. \quad (10)$$

Next we replace the b_0 in (P-B) with this estimate and rewrite (P-B) as

$$\begin{aligned} & \underset{W}{\text{minimize}} && \|X - W \cdot X\|_F^2, \\ & \text{subject to} && W_{ij} = 0 \text{ if } \text{dist}(x_i, x_j) \notin [l_n, l_n + 1], \end{aligned} \quad (\text{P-W})$$

where $X = Y - \hat{A} \cdot \hat{C} - \hat{\mathbf{b}}_0 \mathbf{1}^T$. Given the optimized \hat{W} , our estimation of the fluctuating background is $\hat{B}^f = \hat{W}X$. The new optimization problem (P-W) can be readily parallelized into d linear regression problems for each pixel separately. By estimating all row columns of $W_{i,:}$, we are able to obtain the whole background signal as

$$\hat{B} = \hat{W}X + \hat{\mathbf{b}}_0 \mathbf{1}^T. \quad (11)$$

537 In some cases, X might include large residuals from the inaccurate estimation of the neurons'
 538 spatiotemporal activity AC , e.g., missing neurons in the estimation. These residuals act as outliers
 539 and distort the estimation of \hat{B}^f and b_0 . To overcome this problem, we use robust least squares
 540 regression (RLSR) via hard thresholding to avoid contaminations from the outliers (**Bhatia et al.**,
 541 **2015**). Before solving the problem (P-W), we compute $B^- = \hat{W}(Y - \hat{A} \cdot \hat{C} - \hat{b}_0 \mathbf{1}^T)$ (the current estimate
 542 of the fluctuating background) and then apply a simple clipping preprocessing step to X :

$$X_{it}^{clipped} = \begin{cases} B_{it}^- & \text{if } X_{it} \geq B_{it}^- + \zeta \cdot \sigma_i \\ X_{it} & \text{otherwise} \end{cases}. \quad (12)$$

543 Then we update the regression estimate using $X^{clipped}$ instead of X , and iterate. Here σ_i is the
 544 standard deviation of the noise at x_i and its value can be estimated using the power spectral density
 545 (PSD) method (**Pnevmatikakis et al.**, **2016**). As for the first iteration of the model fitting, we set
 546 each $B_{it}^- = \frac{1}{|\Omega_i|} \sum_{j \in \Omega_i} \tilde{X}_{jt}$ as the mean of the \tilde{X}_{jt} for all $j \in \Omega_i$. The thresholding coefficient ζ can be
 547 specified by users, though we have found a fixed default works well across the datasets used here.
 548 This preprocessing removes most calcium transients by replacing those frames with the previously
 549 estimated background only. As a result, it increases the robustness to inaccurate estimation of AC ,
 550 and in turn leads to a better extraction of AC in the following iterations.

551 Initialization of model variables

552 Since problem (P-All) is not convex in all of its variables, a good initialization of model variables is
 553 crucial for fast convergence and accurate extraction of all neurons' spatiotemporal activity. Previous
 554 methods assume the background component is relatively weak, allowing us to initialize \hat{A} and \hat{C}
 555 while ignoring the background or simply initializing it with a constant baseline over time. However,
 556 the noisy background in microendoscopic data fluctuates more strongly than the neural signals (c.f.
 557 Figure 6C and Figure 7B), which makes previous methods less valid for the initialization of CNMF-E.

558 Here we design a new algorithm to initialize \hat{A} and \hat{C} without estimating \hat{B} . The whole procedure
 559 is illustrated in Figure 10 and described in Algorithm 1. The key aim of our algorithm is to exploit
 560 the relative spatial smoothness in the background compared to the single neuronal signals visible
 561 in the focal plane. Thus we can use spatial filtering to reduce the background in order to estimate
 562 single neurons' temporal activity, and then initialize each neuron's spatial footprint given these
 563 temporal traces. Once we have initialized \hat{A} and \hat{C} , it is straightforward to initialize the constant
 564 baseline b_0 and the fluctuating background B^f by solving problem (P-B).

565 Spatially filtering the data

566 We first filter the raw video data with a customized image kernel (Figure 10A). The kernel is generated
 567 from a Gaussian filter

$$h(\mathbf{x}) = \exp\left(-\frac{\|\mathbf{x}\|^2}{2(l/4)^2}\right). \quad (13)$$

568 Here we use $h(\mathbf{x})$ to approximate a cell body; the factor of $1/4$ in the Gaussian width is chosen to
 569 match a Gaussian shape to a cell of width l . Instead of using $h(\mathbf{x})$ as the filtering kernel directly,
 570 we subtract its spatial mean (computed over a region of width equal to l) and filter the raw data
 571 with $\tilde{h}(\mathbf{x}) = h(\mathbf{x}) - \bar{h}(\mathbf{x})$. The filtered data is denoted as $Z \in \mathbb{R}^{d \times T}$ (Figure 10B). This spatial filtering
 572 step helps accomplish two goals: (1) reducing the background B , so that Z is dominated by neural
 573 signals (albeit somewhat spatially distorted) in the focal plane (see Figure 10B as an example); (2)
 574 performing a template matching to detect cell bodies similar to the Gaussian kernel. Consequently,
 575 Z has large values near the center of each cell body. (However, note that we can not simply e.g.
 576 apply CNMF to Z , because the spatial components in a factorization of the matrix Z will typically
 577 no longer be nonnegative, and therefore NMF-based approaches can not be applied directly.) More
 578 importantly, the calcium traces near the neuron center in the filtered data preserve the calcium
 579 activity of the corresponding neurons because the filtering step results in a weighted average of
 580 cellular signals surrounding each pixel (Figure 10B). Thus the fluorescence traces in pixels close to

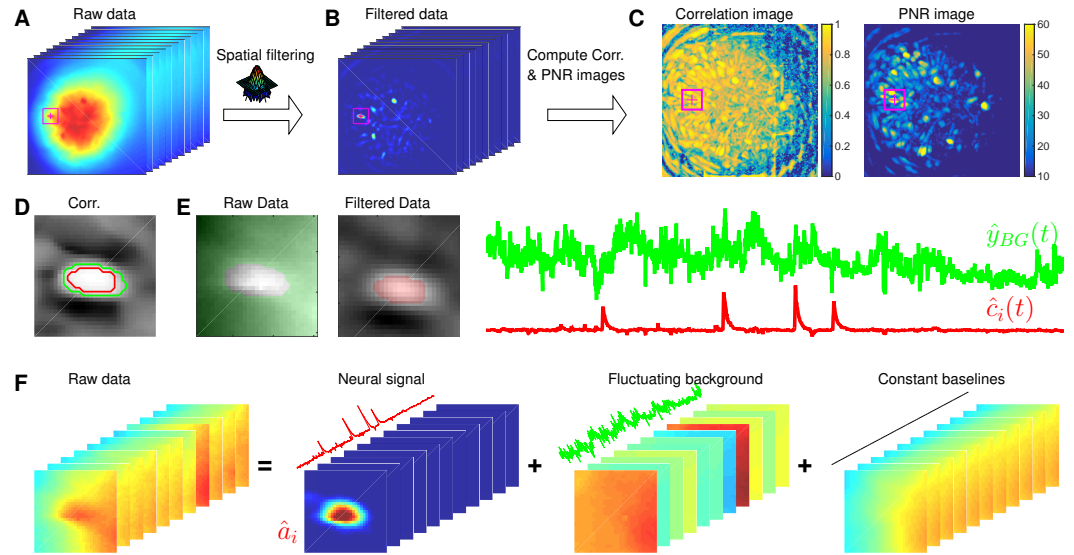


Figure 10. Illustration of the initialization procedure. **(A)** Raw video data and the kernel for filtering the video data. **(B)** The spatially high-pass filtered data. **(C)** The local correlation image and the peak-to-noise ratio (PNR) image calculated from the filtered data in **(B)**. **(D)** The temporal correlation coefficients between the filtered traces **(B)** of the selected seed pixel (the red cross) and all other pixels in the cropped area as shown in **(A-C)**. The red and green contour correspond to correlation coefficients equal to 0.7 and 0.3 respectively. **(E)** The estimated background fluctuation $y_{BG}(t)$ (green) and the initialized temporal trace $\hat{c}_i(t)$ of the neuron (red). $y_{BG}(t)$ is computed as the median of the raw fluorescence traces of all pixels (green area) outside of the green contour shown in **(D)** and $\hat{c}_i(t)$ is computed as the mean of the filtered fluorescence traces of all pixels inside the red contour. **(F)** The decomposition of the raw video data within the cropped area. Each component is a rank-1 matrix and the related temporal traces are estimated in **(E)**. The spatial components are estimated by regressing the raw video data against these three traces. See [S3 Video](#) for an illustration of the initialization procedure.

581 neuron centers in Z can be used for initializing the neurons' temporal activity directly. These pixels
582 are defined as seed pixels. We next propose a quantitative method to rank all potential seed pixels.

583 Ranking seed pixels

584 A seed pixel x should have two main features: first, $Z(x)$, which is the filtered trace at pixel x , should
585 have high peak-to-noise ratio (PNR) because it encodes the calcium concentration c_i of one neuron;
586 second, a seed pixel should have high temporal correlations with its neighboring pixels (e.g., 4
587 nearest neighbors) because they share the same c_i . We computed two metrics for each of these
588 two features:

$$P(x) = \frac{\max_t(Z(x,t))}{\sigma(x)}, \quad L(x) = \frac{1}{4} \sum_{\text{dist}(x,x')=1} \text{corr}(Z(x), Z(x')). \quad (14)$$

589 Recall that $\sigma(x)$ is the standard deviation of the noise at pixel x ; the function **corr()** refers to Pearson
590 correlation here. In our implementation, we usually threshold $Z(x)$ by $3\sigma(x)$ before computing $L(x)$
591 to reduce the influence of the background residuals, noise, and spikes from nearby neurons.

592 Most pixels can be ignored when selecting seed pixels because their local correlations or PNR
593 values are too small. To avoid unnecessary searches of the pixels, we set thresholds for both
594 $P(x)$ and $L(x)$, and only pick pixels larger than the thresholds P_{\min} and L_{\min} . It is empirically useful
595 to combine both metrics for screening seed pixels. For example, high PNR values could result
596 from large noise, but these pixels usually have small $L(x)$ because the noise is not shared with
597 neighboring pixels. On the other hand, insufficient removal of background during the spatial
598 filtering leads to high $L(x)$, but the corresponding $P(x)$ are usually small because most background
599 fluctuations have been removed. So we create another matrix $R(x) = P(x) \cdot L(x)$ that computes the
600 pixelwise product of $P(x)$ and $L(x)$. We rank all $R(x)$ in a descending order and choose the pixel x^*
601 with the largest $R(x)$ for initialization.

Algorithm 1 Initialize model variables A and C given the raw data

Require: data $Y \in \mathbb{R}^{d \times T}$, neuron size l , the minimum local correlation L_{min} and the minimum PNR P_{min} for selecting seed pixels.

- 1: $h \leftarrow$ a truncated 2D Gaussian kernel of width $\sigma_x = \sigma_y = \frac{l}{4}$; $h \in \mathbb{R}^{l \times l}$ ▷ 2D Gaussian kernel
- 2: $\bar{h} \leftarrow h - \bar{h}$; $\bar{h} \in \mathbb{R}^{l \times l}$ ▷ mean-centered kernel for spatial filtering
- 3: $Z \leftarrow \text{conv}(Y, h)$; $Z \in \mathbb{R}^{d \times T}$ ▷ spatially filter the raw data
- 4: $L \leftarrow$ local cross-correlation image of the filtered data Z ; $L \in \mathbb{R}^d$
- 5: $P \leftarrow$ PNR image of the filtered data Z ; $P \in \mathbb{R}^d$
- 6: $k \leftarrow 0$ ▷ neuron number
- 7: **while** True **do**
- 8: **if** $L(x) \leq L_{min}$ or $P(x) \leq P_{min}$ for all pixel x **then**
- 9: **break**;
- 10: **else**
- 11: $k \leftarrow k + 1$
- 12: $\hat{a}_k \leftarrow \mathbf{0}; a \in \mathbb{R}^d$
- 13: $x^* \leftarrow \text{argmax}_x(L(x) \cdot P(x))$ ▷ select a seed pixel
- 14: $\Omega_k \leftarrow \{x|x \text{ is in the square box of length } (2l + 1) \text{ surrounding pixel } x^*\}$ ▷ crop a small box near x^*
- 15: $r(x) \leftarrow \text{corr}(Z(x, :), Z(x^*, :))$ for all $x \in \Omega_k$; $r \in \mathbb{R}^{|\Omega_k|}$
- 16: $y_{BG} \leftarrow \frac{\sum_{\{x|r(x) \leq 0.3\}} Y(x,:)}{\sum_{\{x|r(x) \leq 0.3\}} 1}$; $y_{BG} \in \mathbb{R}^T$ ▷ estimate the background signal
- 17: $\hat{c}_k \leftarrow \frac{\sum_{\{x|r(x) \geq 0.7\}} Z(x,:)}{\sum_{\{x|r(x) \geq 0.7\}} 1}$; $\hat{c}_k \in \mathbb{R}^T$ ▷ estimate neural signal
- 18: $\hat{a}_k(\Omega_k), \hat{b}^{(f)}, \hat{b}^{(0)} \leftarrow \text{argmin}_{a,b^{(f)},b^{(0)}} \|Y_{\Omega_k} - (a \cdot \hat{c}_k^T + b^{(f)} \cdot y_{BG}^T + b^{(0)} \cdot \mathbf{1}^T)\|_F^2$
- 19: $\hat{a}_k \leftarrow \max(0, \hat{a}_k)$ ▷ the spatial component of the k -th neuron
- 20: $Y \leftarrow Y - \hat{a}_k \cdot \hat{c}_k^T$ ▷ peel away the neuron's spatiotemporal activity
- 21: update $L(x)$ and $P(x)$ locally given the new Y
- 22: $A \leftarrow [\hat{a}_1, \hat{a}_2, \dots, \hat{a}_k]$
- 23: $C \leftarrow [\hat{c}_1, \hat{c}_2, \dots, \hat{c}_k]^T$
- 24: **return** A, C

602 Greedy initialization

603 Our initialization method greedily initializes neurons one by one. Every time we initialize a neuron,
 604 we will remove its initialized spatiotemporal activity from the raw video data and initialize the next
 605 neuron from the residual. For the same neuron, there are several seed pixels that could be used
 606 to initialize it. But once the neuron has been initialized from any of these seed pixels (and the
 607 spatiotemporal residual matrix has been updated by peeling away the corresponding activity), the
 608 remaining seed pixels related to this neuron have lowered PNR and local correlation. This helps
 609 avoid the duplicate initialization of the same neuron. Also, $P(x)$ and $L(x)$ have to be updated after
 610 each neuron is initialized, but since only a small area near the initialized neuron is affected, we can
 611 update these quantities locally to reduce the computational cost. This procedure is repeated until
 612 the specified number of neurons have been initialized or no more candidate seed pixels exist.

613 This initialization algorithm can greedily initialize the required number of neurons, but the
 614 subproblem of estimating \hat{a}_i given \hat{c}_i still has to deal with the large background activity in the
 615 residual matrix. We developed a simple method to remove this background and accurately initialize
 616 neuron shapes, described next. We first crop a $(2l + 1) \times (2l + 1)$ square centered at x^* in the field
 617 of view (Figure 10A-E). Then we compute the temporal correlation between the filtered traces of
 618 pixel x^* and all other pixels in the patch (Figure 10D). We choose those pixels with small temporal
 619 correlations (e.g., 0.3) as the neighboring pixels that are outside of the neuron (the green contour in
 620 Figure 10D). Next, we estimate the background fluctuations as the median values of these pixels
 621 for each frame in the raw data (Figure 10E). We also select pixels that are within the neuron by
 622 selecting correlation coefficients larger than 0.7, then \hat{c}_i is refined by computing the mean filtered
 623 traces of these pixels (Figure 10E). Finally, we regress the raw fluorescence signal in each pixel onto
 624 three sources: the neuron signal (Figure 10E), the local background fluctuation (Figure 10F), and a
 625 constant baseline. Our initial estimate of \hat{a}_i is given by the regression weights onto \hat{c}_i in Figure 10F.

626 Modifications for high temporal or spatial correlation
 627 The above procedure works well in most experimental datasets as long as neurons are not highly
 628 spatially overlapped and temporally correlated. However, in a few extreme cases, this initialization
 629 may lead to bad local minima. We found that two practical modifications can lead to improved
 630 results.

631 **High temporal correlation, low spatial overlaps:** The greedy initialization procedure assumes
 632 that closeby neurons are not highly correlated. If this assumption fails, CNMF-E will first merge
 633 nearby neurons into one component for explaining the shared fluctuations, and then the following
 634 initialized components will only capture the residual signals of each neuron. Our solution to this
 635 issue relies on our accurate background removal procedure, after which we simply re-estimate each
 636 neural trace c_i as a weighted fluorescence trace of the background-subtracted video ($Y - \hat{B}^f - \hat{b}_0 \mathbf{1}^T$),

$$\hat{c}_i = \frac{\tilde{\mathbf{a}}_i^T \cdot (Y - \hat{B}^f - \hat{b}_0 \mathbf{1}^T)}{\tilde{\mathbf{a}}_i^T \cdot \tilde{\mathbf{a}}_i}, \quad (15)$$

637 where $\tilde{\mathbf{a}}_i$ only selects pixels with large weights by thresholding the estimated $\hat{\mathbf{a}}_i$ with $\max(\hat{\mathbf{a}}_i)/2$ (this
 638 reduces the contributions from smaller neighboring neurons). This strategy improves the extraction
 639 of individual neurons' traces in the high correlation scenarios and the spatial footprints can be
 640 corrected in the following step of updating \hat{A} . Figure 4B and Figure 5 illustrate this procedure.

641 **High spatial overlaps, low temporal correlation:** CNMF-E may initialize components with
 642 shared temporal traces because they have highly overlapping areas. We solve this problem by
 643 de-correlating their traces (following a similar approach in (*Pnevmatikakis et al., 2016*)). We start
 644 by assuming that neurons with high spatial overlap do not fire spikes within the same frame. If so,
 645 only the inferred spiking trace with the largest value is kept and the rest will be set to 0. Then we
 646 initialize each c_i given these thresholded spiking traces and the corresponding AR coefficients.

647 Interventions

648 We use iterative matrix updates to estimate model variables in CNMF-E. This strategy gives us the
 649 flexibility of integrating prior information on neuron morphology and temporal activity during the
 650 model fitting. The resulting interventions (which can in principle be performed either automatically
 651 or under manual control) can in turn lead to faster convergence and more accurate source extraction.
 652 We integrate 5 interventions in our CNMF-E implementation. Following these interventions, we
 653 usually run one more iteration of matrix updates.

654 Merge existing components

655 When a single neuron is split mistakenly into multiple components, a merge step is necessary to
 656 rejoin these components. If we can find all split components, we can superimpose all their spa-
 657 tiotemporal activities and run rank-1 NMF to obtain the spatial and temporal activity of the merged
 658 neuron. We automatically merge components for which the spatial and temporal components are
 659 correlated above certain thresholds. Our code also provides methods to manually specify neurons
 660 to be merged based on human judgment.

661 Split extracted components

662 When highly correlated neurons are mistakenly merged into one component, we need to use spatial
 663 information to split into multiple components according to neurons' morphology. Our current
 664 implementation of component splitting requires users to manually draw ROIs for splitting the
 665 spatial footprint of the extracted component. Automatic methods for ROI segmentation (*Apthorpe*
et al., 2016; Pachitariu et al., 2013) could be added as an alternative in future implementations.

667 Remove false positives

668 Some extracted components have spatial shapes that do not correspond to real neurons or tempo-
 669 ral traces that do not correspond to neural activity. These components might explain some neural
 670 signals or background activity mistakenly. Our source extraction can benefit from the removal of

671 these false positives. This can be done by manually examining all extracted components, or in prin-
 672 ciple automatically by training a classifier for detecting real neurons. The current implementation
 673 relies on visual inspection to exclude false positives. We also rank neurons based on their SNRs and
 674 set a cutoff to discard all extracted components that fail to meet this cutoff. As with the splitting
 675 step, removing false positives could also potentially use automated ROI detection algorithms in the
 676 future. See [S10 Video](#) for an example involving manual merge and delete operations.

677 Pick undetected neurons from the residual
 678 If all neural signals and background are accurately estimated, the residual of the CNMF-E model
 679 $Y_{\text{res}} = Y - \hat{A}\hat{C} - \hat{B}$ should be relatively spatially and temporally uncorrelated. However, the initializa-
 680 tion might miss some neurons due to large background fluctuations and/or high neuron density.
 681 After we estimate the background \hat{B} and extract a majority of the neurons, those missed neurons
 682 have prominent fluorescent signals left in the residual. To select these undetected neurons from
 683 the residual Y_{res} , we use the same algorithm as for initializing neurons from the raw video data, but
 684 typically now the task is easier because the background has been removed.

685 Post-process the spatial footprints

686 Each single neuron has localized spatial shapes and including this prior into the model fitting of
 687 CNMF-E, as suggested in (*Pnevmatikakis et al., 2016*), leads to better extraction of spatial footprints.
 688 In the model fitting step, we constrain A to be sparse and spatially localized. These constraints
 689 do give us compact neuron shapes in most cases, but in some cases there are still some visually
 690 abnormal components detected. We include a heuristic automated post-processing step after
 691 each iteration of updating spatial shapes (P-S). For each extracted neuron $A(:, k)$, we first convert
 692 it to a 2D image and perform morphological opening to remove isolated pixels resulting from
 693 noise (*Haralick et al., 1987*). Next we label all connected components in the image and create
 694 a mask to select the largest component. All pixels outside of the mask in $A(:, i)$ are set to be 0.
 695 This post-processing induces compact neuron shapes by removing extra pixels and helps avoid
 696 mistakenly explaining the fluorescence signals of the other neurons.

697 Further algorithmic details

698 The simplest pipeline for running CNMF-E includes the following steps:

- 699 1. Initialize \hat{A}, \hat{C} using the proposed initialization procedure.
- 700 2. Solve problem (P-B) for updates of \hat{b}_0 and \hat{B}^f .
- 701 3. Iteratively solve problem (P-S) and (P-T) to update \hat{A}, \hat{C} and \hat{b}_0 .
- 702 4. If desired, apply interventions to intermediate results.
- 703 5. Repeat steps 2, 3, and 4 until the inferred components are stable.

704 In practice, the estimation of the background B (step 2) often does not vary greatly from iteration to
 705 iteration and so this step usually can be run with fewer iterations to save time. In practice, we also
 706 use spatial and temporal decimation for improved speed, following (*Friedrich et al., 2017a*). We
 707 first run the pipeline on decimated data to get good initializations, then we up-sample the results
 708 \hat{A}, \hat{C} to the original resolution and run one iteration of steps (2-3) on the raw data. This strategy
 709 improves on processing the raw data directly because downsampling increases the signal to noise
 710 ratio and eliminates many false positives.

711 Step 4 provides a fast method for correcting abnormal components without redoing the whole
 712 analysis. (This is an important improvement over the PCA/ICA pipeline, where if users encounter
 713 poor estimated components it is necessary to repeat the whole analysis with new parameter values,
 714 which may not necessarily yield improved cell segmentations.) The interventions described here
 715 themselves can be independent tasks in calcium imaging analysis; with further work we expect many
 716 of these steps can be automated. In our interface for performing manual interventions, the most
 717 frequently used function is to remove false positives. Again, components can be rejected following

Name	Description	Default Values	Used in
I	size of a typical neuron soma in the FOV	$30\mu m$	Algorithm 1
I_n	the distance between each pixel and its neighbors	$60\mu m$	Problem (P-B)
P_{\min}	the minimum peak-to-noise ratio of seed pixels	10	Algorithm 1
L_{\min}	the minimum local correlation of seed pixels	0.8	Algorithm 1
ζ	the ratio between the outlier threshold and the noise	10	Problem (P-B)

Table 2. Optional user-specified parameters.

718 visual inspection in PCA/ICA analysis, but the performance of CNMF-E can be improved with further
 719 iterations after removing false positives, while this is not currently an option for PCA/ICA.

720 We have also found a two-step initialization procedure useful for detecting neurons: we first
 721 start from relatively high thresholds of P_{\min} and L_{\min} to initialize neurons with large activity from the
 722 raw video data; then we estimate the background components by solving problem (P-B); finally we
 723 can pick undetected neurons from the residual using smaller thresholds. We can terminate the
 724 model iterations when the residual sum of squares (RSS) stabilizes (see Figure 4B), but this is seldom
 725 used in practice because computing the RSS is time-consuming. Instead we usually automatically
 726 stop the iterations after the number of detected neurons stabilizes. If manual interventions are
 727 performed, we typically run one last iteration of updating B , A and C sequentially to further refine
 728 the results.

729 Parameter selection

730 Table 2 shows 5 key parameters used in CNMF-E. All of these parameters have interpretable meaning
 731 and can be easily picked within a broad range. The parameter I controls the size of the spatial filter
 732 in the initialization step and is chosen as the diameter of a typical neuron in the FOV. As long as I
 733 is much smaller than local background sources, the filtered data can be used for detecting seed
 734 pixels and then initializing neural traces. The distance between each seed pixel and its selected
 735 neighbors I_n has to be larger than the neuron size I and smaller than the spatial range of local
 736 background sources; in practice, this range is fairly broad. We usually set I_n as $2I$. To determine the
 737 thresholds P_{\min} and L_{\min} , we first compute the correlation image and PNR image and then visually
 738 select very weak neurons from these two images. P_{\min} and L_{\min} are determined to ensure that
 739 CNMF-E is able to choose seed pixels from these weak neurons. Small P_{\min} and L_{\min} yield more false
 740 positive neurons, but they can be removed in the intervention step. Finally, in practice, our results
 741 are not sensitive to the selection of the outlier parameter ζ , thus we frequently set it as 10.

742 Complexity analysis

743 In step 1, the time cost is mainly determined by spatial filtering, resulting in $O(dT)$ time. As for the
 744 initialization of a single neuron given a seed pixel, it is only ($O(T)$). Considering the fact that the
 745 number of neurons is typically much smaller than the number of pixels in this data, the complexity
 746 for step 1 remains $O(dT)$. In step 2, the complexity of estimating \hat{b}_0 is $O(dT)$ and estimating \hat{B}^f scales
 747 linearly with the number of pixels d . For each pixel, the computational complexity for estimating
 748 $W_{i,:}$ is $O(T)$. Thus the computational complexity in updating the background component is $O(dT)$.
 749 In step 3, the computational complexities of solving problems (P-S) and (P-T) have been discussed
 750 in previous literature (Pnevmatikakis et al., 2016) and they scale linearly with pixel number d and
 751 time T , i.e., $O(dT)$. For the interventions, the one with the largest computational cost is picking
 752 undetected neurons from the residual, which is the same as the initialization step. Therefore, the
 753 computational cost for step 4 is $O(dT)$. To summarize, the complexity for running CNMF-E is $O(dT)$,
 754 i.e. the method scales linearly with both the number of pixels and the total recording time.

Dataset	Striatum	PFC	Hippocampus	BNST
Size ($x \times y \times t$)	$256 \times 256 \times 6000$	$175 \times 184 \times 9000$	$175 \times 184 \times 9000$	$175 \times 184 \times 9000$
(# PCs, # ICs)	(2000, 700)	(275, 250)	(100, 50)	(200, 150)
PFC/ICA	986	181	174	53
CNMF-E	726	221	335	435

Table 3. Running time (sec) for processing the 4 experimental datasets.755 **Implementations**

756 Our MATLAB implementation supports running CNMF-E in three different modes that are optimized
 757 for different datasets: single-mode, patch-mode and multi-batch-mode.

758 Single-mode is a naive implementation that loads data into memory and fits the model. It is fast
 759 for processing small datasets (< 1GB).

760 For larger datasets, many computers have insufficient RAM for loading all data into memory
 761 and storing intermediate results. Patch-mode CNMF-E divides the whole FOV into multiple small
 762 patches and maps data to the hard drive (*Giovannucci et al., 2017b*). The data within each patch are
 763 loaded only when we process that patch. This significantly reduces the memory consumption. More
 764 importantly, this mode allows running CNMF-E in parallel on multi-core CPUs, yielding a speed-up
 765 roughly proportional to the number of available cores.

766 Multi-batch mode builds on patch-mode, and is optimized for even larger datasets, especially
 767 data collected over multiple sessions/days. This mode segments data into multiple batches tem-
 768 porally and assumes that the neuron footprints A are shared across all batches. We process each
 769 batch using patch mode and perform partial weighted updates on A given the traces C obtained in
 770 each batch.

771 All modes also include a logging system for keeping track of manual interventions and interme-
 772 diate operations.

773 The Python implementation is similar; see (*Giovannucci et al., 2017b*) for full details.

774 **Running time**

775 To provide a sense of the running time of the different steps of the algorithm, we timed the code on
 776 the simulation data shown in Figure 4. This dataset is 253×316 pixels $\times 2000$ frames. The analyses
 777 were performed on a desktop with Intel Xeon CPU E5-2650 v4 @2.20GHz and 128GB RAM running
 778 Ubuntu 16.04. We used a parallel implementation for performing the CNMF-E analysis, with patch
 779 size 64×64 pixels, using up to 12 cores. PCA/ICA took ~ 211 seconds to converge, using 250 PCs and
 780 220 ICs. CNMF-E spent 55 seconds for initialization, 1 second for merging and deleting components,
 781 110 seconds for the first round of the background estimation and 40 seconds in the following
 782 updates, 8 seconds for picking neurons from the residual, and 10 seconds per iteration for updating
 783 spatial (A) and temporal (C) components, resulting in a total of 258 seconds.

784 Finally, Table 3 shows the running time of processing the four experimental datasets.

785 **Simulation experiments**786 **Details of the simulated experiment of Figure 2**

787 The field of view was 256×256 , with 1000 frames. We simulated 50 neurons whose shapes were
 788 simulated as spherical 2-D Gaussian. The neuron centers were drawn uniformly from the whole FOV
 789 and the Gaussian widths σ_x and σ_y for each neuron was also randomly drawn from $\mathcal{N}(\frac{l}{4}, (\frac{l}{10})^2)$,
 790 where $l = 12$ pixels. Spikes were simulated from a Bernoulli process with probability of spiking per
 791 timebin 0.01 and then convolved with a temporal kernel $g(t) = \exp(-t/\tau_d) - \exp(-t/\tau_r)$, with fall time
 792 $\tau_d = 6$ timebin and rise time $\tau_r = 1$ timebin. We simulated the spatial footprints of local backgrounds
 793 as 2-D Gaussian as well, but the mean Gaussian width is 5 times larger than the neurons' widths. As
 794 for the spatial footprint of the blood vessel in Figure 2A, we simulated a cubic function and then

795 convolved it with a 2-D Gaussian (Gaussian width=3 pixel). We use a random walk model to simulate
 796 the temporal fluctuations of local background and blood vessel. For the data used in Figure 2A-H,
 797 there were 23 local background sources; for Figure 2I, we varied the number of background sources.

798 We used the raw data to estimate the background in CNMF-E without subtracting the neural
 799 signals $\hat{A}\hat{C}$ in problem (P-B). We set $I_n = 15$ pixels and left the remaining parameters at their default
 800 values. The plain NMF was performed using the built-in MATLAB function nnmf, which utilizes
 801 random initialization.

802 Details of the simulated experiment of Figure 3, Figure 4 and Figure 5
 803 We used the same simulation settings for both Figure 3 and Figure 4. The field of view was 253×316
 804 and the number of frames was 2000. We simulated 200 neurons using the same method as the
 805 simulation in Figure 2, but for the background we used the spatiotemporal activity of the background
 806 extracted using CNMF-E from real experimental data (data not shown). The noise level Σ was also
 807 estimated from the data. When we varied the SNR in Figure 4D-G, we multiplied Σ with an SNR
 808 reduction factor.

809 We set $I = 12$ pixels to create the spatial filtering kernel. As for the thresholds used for determining
 810 seed pixels, we varied them for different SNR settings by visually checking the corresponding
 811 local correlation images and PNR images. The selected values were $L_{\min} = [0.9, 0.8, 0.8, 0.8, 0.6, 0.6]$
 812 and $P_{\min} = [15, 10, 10, 8, 6, 6]$ for different SNR reduction factors [1, 2, 3, 4, 5, 6]. For PCA/ICA analysis,
 813 we set the number of PCs and ICs as 600 and 300 respectively.

814 The simulation in Figure 5 only includes 2 neurons (as seen in Figure 3E) using the same
 815 simulation parameters. We replaced their temporal traces c_1 and c_2 with $(1 - \rho)c_1 + \rho c_3$ and $(1 -$
 816 $\rho)c_2 + \rho c_3$, where ρ is tuned to generate different correlation levels (γ), and c_3 is simulated in the
 817 same way as c_1 and c_2 . We also added a new background source whose temporal profile is c_3 to
 818 increase the neuron-background correlation as ρ increases. CNMF-E was run as in Figure 4. We
 819 used 20 PCs and ICs for PCA/ICA.

820 ***In vivo* microendoscopic imaging and data analysis**

821 For all experimental data used in this work, we ran both CNMF-E and PCA/ICA. For CNMF-E, we
 822 chose parameters so that we initialized about 10-20% extra components, which were then merged
 823 or deleted (some automatically, some under manual supervision) to obtain the final estimates.
 824 Exact parameter settings are given for each dataset below. For PCA/ICA, the number of ICs were
 825 selected to be slightly larger than our extracted components in CNMF-E (as we found this led to
 826 the best results for this algorithm), and the number of PCs was selected to capture over 90% of the
 827 signal variance. The weight of temporal information in spatiotemporal ICA was set as 0.1. After
 828 obtaining PCA/ICA filters, we again manually removed components that were clearly not neurons
 829 based on neuron morphology.

830 We computed the SNR of extracted cellular traces to quantitatively compare the performances
 831 of two approaches. For each cellular trace y , we first computed its denoised trace c using the
 832 selected deconvolution algorithm (here, it is thresholded OASIS); then the SNR of y is

$$833 \text{SNR} = \frac{\|c\|_2^2}{\|y - c\|_2^2}. \quad (16)$$

834 For PCA/ICA results, the calcium signal y of each IC is the output of its corresponding spatial filter,
 835 while for CNMF-E results, it is the trace before applying temporal deconvolution, i.e., \hat{y}_i in Eq. (9). All
 836 the data can be freely accessed online Zhou et al. (2017).

837 **Dorsal striatum data**

838 Expression of the genetically encoded calcium indicator GCaMP6f in neurons was achieved using a
 839 recombinant adeno-associated virus (AAV) encoding the GCaMP6f protein under transcriptional
 840 control of the synapsin promoter (AAV-Syn-GCaMP6f). This viral vector was packaged (Serotype 1)

840 and stored in undiluted aliquots at a working concentration of > 1012 genomic copies per ml at
 841 -80°C until intracranial injection. 500 μ l of AAV1-Syn-GCaMP6f was injected unilaterally into dorsal
 842 striatum (0.6 mm anterior to Bregma, 2.2mm lateral to Bregma, 2.5mm ventral to the surface of the
 843 brain). 1 week post injection, a 1mm gradient index of refraction (GRIN) lens was implanted into
 844 dorsal striatum ~ 300 μ m above the center of the viral injection. 3 weeks after the implantation, the
 845 GRIN lens was reversibly coupled to a miniature 1-photon microscope with an integrated 475nm
 846 LED (Inscopix). Using nVistaHD Acquisition software, images were acquired at 30 frames per second
 847 with the LED transmitting 0.1 to 0.2 mW of light while the mouse was freely moving in an open
 848 field arena. Images were down sampled to 10Hz and processed into TIFFs using Mosaic software.
 849 All experimental manipulations were performed in accordance with protocols approved by the
 850 Harvard Standing Committee on Animal Care following guidelines described in the US NIH Guide
 851 for the Care and Use of Laboratory Animals.

852 The parameters used in running CNMF-E were: $I = 13$ pixels, $I_n = 18$ pixels, $L_{\min} = 0.7$, and
 853 $P_{\min} = 7$. 728 components were initialized from the raw data in the first pass before subtracting the
 854 background, and then additional components were initialized in a second pass. Highly-correlated
 855 nearby components were merged and false positives were removed using the automated approach
 856 described above. In the end, we obtained 692 components.

857 Prefrontal cortex data

858 Cortical neurons were targeted by administering 2 microinjections of 300 ul of AAV-DJ-CamkIIa-
 859 GCaMP6s (titer: 5.3 x 1012, 1:6 dilution, UNC vector core) into the prefrontal cortex (PFC) (coordi-
 860 nates relative to bregma; injection 1: +1.5 mm AP, 0.6 mm ML, -2.4 ml DV; injection 2: +2.15 AP, 0.43
 861 mm ML, -2.4 mm DV) of an adult male wild type (WT) mice. Immediately following the virus injection
 862 procedure, a 1 mm diameter GRIN lens implanted 300 um above the injection site (coordinates
 863 relative to bregma: +1.87 mm AP, 0.5 mm ML, -2.1 ml DV). After sufficient time had been allowed for
 864 the virus to express and the tissue to clear underneath the lens (3 weeks), a baseplate was secured
 865 to the skull to interface the implanted GRIN lens with a miniature, integrated microscope (nVista,
 866 473 nm excitation LED, Inscopix) and subsequently permit the visualization of Ca²⁺ signals from
 867 the PFC of a freely behaving mouse. The activity of PFC neurons were recorded at 15 Hz over a
 868 10 min period (nVista HD Acquisition Software, Inscopix) while the test subject freely explored an
 869 empty novel chamber. Acquired data was spatially down sampled by a factor of 2, motion corrected,
 870 and temporally down sampled to 15 Hz (Mosaic Analysis Software, Inscopix). All procedures were
 871 approved by the University of North Carolina Institutional Animal Care and Use Committee (UNC
 872 IACUC).

873 The parameters used in running CNMF-E were: $I = 13$ pixels, $I_n = 18$ pixels, $L_{\min} = 0.9$, and
 874 $P_{\min} = 15$. There were 169 components initialized in the first pass and we obtained 225 components
 875 after running the whole CNMF-E pipeline.

876 Ventral hippocampus data

877 The calcium indicator GCaMP6f was expressed in ventral hippocampal-amygdala projecting neurons
 878 by injecting a retrograde canine adeno type 2-Cre virus (CAV2-Cre; from Larry Zweifel, University
 879 of Washington) into the basal amygdala (coordinates relative to bregma: -1.70 AP, 3.00mm ML,
 880 and -4.25mm DV from brain tissue at site), and a Cre-dependent GCaMP6f adeno associated virus
 881 (AAV1-flex-Synapsin-GCaMP6f, UPenn vector core) into ventral CA1 of the hippocampus (coordinates
 882 relative to bregma: -3.16mm AP, 3.50mm ML, and -3.50mm DV from brain tissue at site). A 0.5mm
 883 diameter GRIN lens was then implanted over the vCA1 subregion and imaging began 3 weeks after
 884 surgery to allow for sufficient viral expression. Mice were then imaged with Inscopix miniaturized
 885 microscopes and nVistaHD Acquisition software as described above; images were acquired at 15
 886 frames per second while mice explored an anxiogenic Elevated Plus Maze arena. Videos were motion
 887 corrected and spatially downsampled using Mosaic software. All procedures were performed in
 888 accordance with protocols approved by the New York State Psychiatric Institutional Animal Care

889 and Use Committee following guidelines described in the US NIH Guide for the Care and Use of
 890 Laboratory Animals.

891 The parameters used in running CNMF-E were: $I = 15$ pixels, $I_n = 30$ pixels, $\zeta = 10$, $L_{\min} = 0.9$,
 892 and $P_{\min} = 15$. We first temporally downsampled the data by 2. Then we applied CNMF-E to
 893 the downsampled data. There were 53 components initialized. After updating the background
 894 component, the algorithm detected 6 more neurons from the residual. We merged most of
 895 these components and deleted false positives. In the end, there were 24 components left. The
 896 intermediate results before and after each manual intervention are shown in [S10 Video](#).

897 BNST data with footshock

898 Calcium indicator GCaMP6s was expressed within CaMKII-expressing neurons in the BNST by
 899 injecting the recombinant adeno-associated virus AAVdj-CaMKII-GCaMP6s (packaged at UNC Vector
 900 Core) into the anterior dorsal portion of BNST (coordinates relative to bregma: 0.10mm AP, -0.95mm
 901 ML, -4.30mm DV). A 0.6 mm diameter GRIN lens was implanted above the injection site within the
 902 BNST. As described above, images were acquired using a detachable miniature 1-photon microscope
 903 and nVistaHD Acquisition Software (Inscopix). Images were acquired at 20 frames per second while
 904 the animal was freely moving inside a sound-attenuated chamber equipped with a house light and
 905 a white noise generator (Med Associates). Unpredictable foot shocks were delivered through metal
 906 bars in the floor as an aversive stimulus during a 10-min session. Each unpredictable foot shock
 907 was 0.75 mA in intensity and 500 ms in duration on a variable interval (VI-60). As described above,
 908 images were motion corrected, downsampled and processed into TIFFs using Mosaic Software.
 909 These procedures were conducted in adult C57BL/6J mice (Jackson Laboratories) and in accordance
 910 with the Guide for the Care and Use of Laboratory Animals, as adopted by the NIH, and with
 911 approval from the Institutional Animal Care and Use Committee of the University of North Carolina
 912 at Chapel Hill (UNC).

913 The parameters used in running CNMF-E were: $I = 15$ pixels, $I_n = 23$ pixels, $\zeta = 10$, $L_{\min} = 0.9$, and
 914 $P_{\min} = 15$. There were 149 components initialized and we detected 29 more components from the
 915 residual after estimating the background. there were 127 components left after running the whole
 916 pipeline.

917 Code availability

918 All analyses was performed with custom-written MATLAB code. MATLAB implementations of
 919 the CNMF-E algorithm can be freely downloaded from https://github.com/zhoupC/CNMF_E (Zhou,
 920 2017a). We also implemented CNMF-E as part of the Python package CalmAn ([Giovannucci et al., 2017b](#)), a computational analysis toolbox for large scale calcium imaging and behavioral data
 921 (<https://github.com/simonsfoundation/CalmAn> ([Giovannucci et al., 2017a](#))).

923 The scripts for generating all figures and the experimental data in this paper can be accessed
 924 from https://github.com/zhoupC/eLife_submission(Zhou, 2017b).

925 Supporting information

926 **S1 Video. An example of typical microendoscopic data.** The video was recorded in dorsal
 927 striatum; experimental details can be found above.

928 [MP4](#)

929 **S2 Video. Comparison of CNMF-E with rank-1 NMF in estimating background fluctuation in
 930 simulated data.** Top left: the simulated fluorescence data in Figure 2. Bottom left: the ground
 931 truth of neuron signals in the simulation. Top middle: the estimated background from the raw
 932 video data (top left) using CNMF-E. Bottom middle: the residual of the raw video after subtracting
 933 the background estimated with CNMF-E. Top right and top bottom: same as top middle and bottom
 934 middle, but the background is estimated with rank-1 NMF.

935 [MP4](#)

936 **S3 Video. Initialization procedure for the simulated data in Figure 3.** Top left: correlation
 937 image of the filtered data. Red dots are centers of initialized neurons. Top middle: candidate seed
 938 pixels (small red dots) for initializing neurons on top of PNR image. The large red dot indicates
 939 the current seed pixel. Top right: the correlation image surrounding the selected seed pixel or the
 940 spatial footprint of the initialized neuron. Bottom: the filtered fluorescence trace at the seed pixel
 941 or the initialized temporal activity (both raw and denoised).

942 [MP4](#)

943 **S4 Video. The results of CNMF-E in demixing simulated data in Figure 4 (SNR reduction fac-
 944 tor=1).** Top left: the simulated fluorescence data. Bottom left: the estimated background. Top
 945 middle: the residual of the raw video (top left) after subtracting the estimated background (bottom
 946 left). Bottom middle: the denoised neural signals. Top right: the residual of the raw video data (top
 947 right) after subtracting the estimated background (bottom left) and denoised neural signal (bottom
 948 middle). Bottom right: the ground truth of neural signals in simulation.

949 [MP4](#)

950 **S5 Video. The results of CNMF-E in demixing the simulated data in Figure 4 (SNR reduction
 951 factor=6).** Conventions as in previous video.

952 [MP4](#)

953 **S6 Video. The results of CNMF-E in demixing dorsal striatum data.** Top left: the recorded
 954 fluorescence data. Bottom left: the estimated background. Top middle: the residual of the raw
 955 video (top left) after subtracting the estimated background (bottom left). Bottom middle: the
 956 denoised neural signals. Top right: the residual of the raw video data (top right) after subtracting
 957 the estimated background (bottom left) and denoised neural signal (bottom middle). Bottom right:
 958 the denoised neural signals while all neurons' activity are coded with pseudocolors.

959 [MP4](#)

960 **S7 Video. The results of CNMF-E in demixing PFC data.** Conventions as in previous video.

961 [MP4](#)

962 **S8 Video. Comparison of CNMF-E with PCA/ICA in demixing overlapped neurons in Figure 7G.**
 963 Top left: the recorded fluorescence data. Bottom left: the residual of the raw video (top left) after
 964 subtracting the estimated background using CNMF-E. Top middle and top right: the spatiotemporal
 965 activity and temporal traces of three neurons extracted using CNMF-E. Bottom middle and bottom
 966 right: the spatiotemporal activity and temporal traces of three neurons extracted using PCA/ICA.

967 [MP4](#)

968 **S9 Video. The results of CNMF-E in demixing ventral hippocampus data.** Conventions as in S6
 969 Video.

970 [MP4](#)

971 **S10 Video. Extracted spatial and temporal components of CNMF-E at different stages (ven-
 972 tral hippocampal dataset).** After initializing components, we ran matrix updates and interventions
 973 in automatic mode, resulting in 32 components in total. In the next iteration, we manually deleted
 974 6 components and automatically merged neurons as well. In the last iterations, 4 neurons were
 975 merged into 2 neurons with manual verifications. The correlation image in the top left panel is
 976 computed from the background-subtracted data in the final step.

977 [MP4](#)

978 **S11 Video. The results of CNMF-E in demixing BNST data.** Conventions as in S6 Video.

979 [MP4](#)

980 Acknowledgments

981 We would like to thank CNMF-E users who received early access to our package and provided
 982 tremendously helpful feedback and suggestions, especially James Hyde, Jesse Wood, and Sean
 983 Piantadosi in Susanne Ahmari's lab in University of Pittsburgh, Andreas Klaus in Rui Costa's Lab in
 984 the Champalimaud Neurobiology of Action Laboratory, Suoqin Jin in Xiangmin Xu's lab at University

985 of California - Irvine, Conor Heins at the National Institute of Drug Abuse, Chris Donahue in Anatol
986 Kreitzer's lab at University of California - San Francisco, Xian Zhang in Bo Li's lab at Cold Spring
987 Harbor Laboratory, Emily Mackevicius in Michale Fee's lab at Massachusetts Institute of Technology,
988 Courtney Cameron and Malavika Murugan in Ilana Witten's lab at Princeton University, Pranav
989 Mamiannan in Jonathan Whitlock's lab at Norwegian University of Science and Technology, and
990 Milekovic Tomislav in Gregoire Courtine's group at EPFL. We also thank Andreas Klaus for valuable
991 comments on the manuscript.

992 **Additional information**

993 **Funding**

Funder	Grant reference	Author
National Institute of Mental Health (NIMH)	2R01MH064537	Robert E. Kass, Pengcheng Zhou
	R37 MH068542	Rene Hen, Jessica C. Jimenez
	R01 MH083862	Rene Hen, Jessica C. Jimenez
	R01 MH108623	Mazen A. Kheirbek
National Institute on Drug Abuse (NIDA)	R90 DA023426	Pengcheng Zhou
	R01 DA038168	Garret D Stuber, Jose Rodriguez-Romaguera
Intelligence Advanced Research Projects Activity (IARPA)	Dol/IBC D16PC00007	Pengcheng Zhou
	Dol/IBC D16PC00003	Liam Paninski
Defense Advanced Research Projects Agency (DARPA)	N66001-15-C-4032	Liam Paninski
Army Research Office (ARO)	MURI W911NF-12-1-0594	Liam Paninski
National Institute of Biomedical Imaging and Bioengineering (NIBIB)	R01 EB22913	Liam Paninski
National Institute of Child Health and Human Development (NICHD)	T32 HD040127	Shanna L. Resendez
	U54-HD079124	Garret D Stuber
Howard Hughes Medical Institute (HHMI)	Gilliam Fellowship for Advanced Study	Jessica C. Jimenez
National Institute on Aging (NIA)	R01 AG043688	Rene Hen, Jessica C. Jimenez
New York State Stem Cell Science (NYSTEM)	NYSTEM-C029157	Rene Hen, Jessica C. Jimenez
Hope For Depression Research Foundation (HDRF)	RGA-13-003	Rene Hen, Jessica C. Jimenez
Canadian Institutes of Health Research (CIHR)	Doctoral Foreign Study Award	Shay Q. Neufeld
The Simons Foundation		Liam Paninski, Garret D Stuber, Andrea Giovannucci, Johannes Friedrich, Eftychios A. Pnevmatikakis
International Mental Health Research Organization (IMHRO)	Rising Star Award	Mazen A. Kheirbek
National Institute of Neurological Disorders and Stroke (NINDS)	U01NS094191	Bernardo L. Sabatini
The funders had no role in study design, data collection and interpretation, or the decision to submit the work for publication.		

994 **References**

- 995 **Apthorpe N, Riordan A, Aguilar R, Homann J, Gu Y, Tank D, Seung HS.** Automatic neuron detection in calcium
996 imaging data using convolutional Networks. In: *Advances in Neural Information Processing Systems* 29; 2016.p.
997 3270-3278.
- 998 **Barbera G, Liang B, Zhang L, Gerfen C, Culurciello E, Chen R, Li Y, Lin DT.** Spatially compact neural clus-

- 999 ters in the dorsal striatum encode locomotion relevant information. *Neuron*. 2016; 92(1):202–213. doi:
 1000 [10.1016/j.neuron.2016.08.037](https://doi.org/10.1016/j.neuron.2016.08.037).
- 1001 **Bhatia K**, Jain P, Kar P. Robust regression via hard thresholding. In: *Advances in Neural Information Processing Systems 28*; 2015.p. 721–729.
- 1003 **Cai DJ**, Aharoni D, Shuman T, Shobe J, Biane J, Lou J, Kim I, Baumgaertel K, Levenstain A, Tuszyński M, Mayford M,
 1004 Silva AJ. A shared neural ensemble links distinct contextual memories encoded close in time. *Nature*. 2016;
 1005 534(7605):115–118. doi: [10.1038/nature17955](https://doi.org/10.1038/nature17955).
- 1006 **Cameron CM**, Pillow J, Witten IB. Cellular resolution calcium imaging and optogenetic excitation reveal a role for
 1007 IL to NAc projection neurons in encoding of spatial information during cocaine-seeking. 2016 Neuroscience
 1008 Meeting Planner San Diego, CA: Society for Neuroscience. 2016; Poster:259.08 / GGG2.
- 1009 **Carvalho Poyraz F**, Holzner E, Bailey MR, Meszaros J, Kenney L, Kheirbek MA, Balsam PD, Kellendonk C. De-
 1010 creasing striatopallidal pathway function enhances motivation by energizing the initiation of goal-directed
 1011 action. *J Neurosci*. 2016; 36(22):5988–6001. doi: [10.1523/JNEUROSCI.0444-16.2016](https://doi.org/10.1523/JNEUROSCI.0444-16.2016).
- 1012 **Cichocki A**, Phan AH. Fast local algorithms for large scale nonnegative matrix and tensor factorizations. *IEICE Transactions on Fundamentals of Electronics, Communications and Computer Sciences*. 2009; E92-A(3):708–
 1013 721. doi: [10.1587/transfun.E92.A.708](https://doi.org/10.1587/transfun.E92.A.708).
- 1015 **Cichocki A**, Zdunek R, Amari Si. Hierarchical ALS algorithms for nonnegative matrix and 3D tensor factorization.
 1016 *Independent Component Analysis and Signal Separation*. 2007; 4666(1):169–176.
- 1017 **Cox J**, Pinto L, Dan Y. Calcium imaging of sleep-wake related neuronal activity in the dorsal pons. *Nature Communications*. 2016; 7:10763. doi: [10.1038/ncomms10763](https://doi.org/10.1038/ncomms10763).
- 1019 **Deneux T**, Kaszas A, Szalay G, Katona G, Lakner T, Grinvald A, Rózsa B, Vanzetta I. Accurate spike estimation
 1020 from noisy calcium signals for ultrafast three-dimensional imaging of large neuronal populations in vivo.
 1021 *Nature Communications*. 2016; 7(August):12190. doi: [10.1038/ncomms12190](https://doi.org/10.1038/ncomms12190).
- 1022 **Dombeck DA**, Graziano MS, Tank DW. Functional clustering of neurons in motor cortex determined by cellular
 1023 resolution imaging in awake behaving mice. *The Journal of neuroscience : the official journal of the Society
 1024 for Neuroscience*. 2009; 29(44):13751–60. doi: [10.1523/JNEUROSCI.2985-09.2009](https://doi.org/10.1523/JNEUROSCI.2985-09.2009).
- 1025 **Donahue CH**, Kreitzer AC. Function of Basal Ganglia Circuitry in Motivation. 2017 Neuroscience Meeting Planner
 1026 Washington, DC: Society for Neuroscience. 2017; Poster.
- 1027 **Flusberg BA**, Nimmerjahn A, Cocker ED, Mukamel EA, Barretto RPJ, Ko TH, Burns LD, Jung JC, Schnitzer MJ. High-
 1028 speed, miniaturized fluorescence microscopy in freely moving mice. *Nature methods*. 2008; 5(11):935–938.
- 1029 **Friedrich J**, Yang W, Soudry D, Mu Y, Ahrens MB, Yuste R, Peterka DS, Paninski L. Multi-scale approaches for high-
 1030 speed imaging and analysis of large neural populations. *PLoS computational biology*. 2017; 13(8):e1005685.
- 1031 **Friedrich J**, Zhou P, Paninski L. Fast online deconvolution of calcium imaging data. *PLOS Computational Biology*.
 1032 2017 03; 13(3):1–26. doi: [10.1371/journal.pcbi.1005423](https://doi.org/10.1371/journal.pcbi.1005423).
- 1033 **Ghosh KK**, Burns LD, Cocker ED, Nimmerjahn A, Ziv Y, Gamal AE, Schnitzer MJ. Miniaturized integration of a
 1034 fluorescence microscope. *Nature Methods*. 2011; 8(10):871–878.
- 1035 **Giovannucci A**, Friedrich J, Deverett B, Staneva V, Chklovskii D, Pnevmatikakis EA, CalmAn. Github; 2017.
 1036 <https://github.com/flatironinstitute/CalmAn>, 6bd51e2.
- 1037 **Giovannucci A**, Friedrich J, Deverett B, Staneva V, Chklovskii D, Pnevmatikakis EA. CalmAn: An open source
 1038 toolbox for large scale calcium imaging data analysis on standalone machines. *Cosyne Abstracts*. 2017; .
- 1039 **Haralick RM**, Sternberg SR, Zhuang X. Image Analysis Using Mathematical Morphology. *IEEE Transactions on
 1040 Pattern Analysis and Machine Intelligence*. 1987; 9(4):532–550. doi: [10.1109/TPAMI.1987.4767941](https://doi.org/10.1109/TPAMI.1987.4767941).
- 1041 **Harrison TC**, Pinto L, Brock JR, Dan Y. Calcium Imaging of Basal Forebrain Activity during Innate and Learned
 1042 Behaviors. *Frontiers in Neural Circuits*. 2016; 10(May):1–12. doi: [10.3389/fncir.2016.00036](https://doi.org/10.3389/fncir.2016.00036).
- 1043 **Jennings JH**, Sparta DR, Stamatakis AM, Ung RL, Pleil KE, Kash TL, Stuber GD. Distinct extended amygdala
 1044 circuits for divergent motivational states. *Nature*. 2013; 496(7444):224–228. doi: [10.1038/nature12041](https://doi.org/10.1038/nature12041).

- 1045 Jennings JH, Ung RL, Resendez SL, Stamatakis AM, Taylor JG, Huang J, Veleta K, Kantak PA, Aita M, Shilling-Scrivo
 1046 K, Ramakrishnan C, Deisseroth K, Otte S, Stuber GD. Visualizing hypothalamic network dynamics for appetitive
 1047 and consummatory behaviors. *Cell*. 2015; 160(3):516–527. doi: [10.1016/j.cell.2014.12.026](https://doi.org/10.1016/j.cell.2014.12.026).
- 1048 Jewell S, Witten D. Exact Spike Train Inference Via ℓ_0 Optimization. arXiv preprint arXiv:170308644. 2017; p.
 1049 1–23.
- 1050 Jimenez JC, Goldberg A, Ordek G, Luna VM, Su K, Pena S, Zweifel L, Hen R, Kheirbek M. Subcortical projection-
 1051 specific control of innate anxiety and learned fear by the ventral hippocampus. 2016 Neuroscience Meeting
 1052 Planner San Diego, CA: Society for Neuroscience. 2016; Poster:455.10 / JJJ26.
- 1053 Jimenez JC, Su K, Goldberg A, Luna VM, Zhou P, Ordek G, Ong S, Zweifel L, Paninski L, Hen R, Kheirbek M. Anxiety
 1054 cells in a hippocampal-hypothalamic circuit. 2017 Neuroscience Meeting Planner Washinton, DC: Society for
 1055 Neuroscience. 2017; Poster.
- 1056 Kitamura T, Sun C, Martin J, Kitch LJ, Schnitzer MJ, Tonegawa S. Entorhinal Cortical Ocean Cells En-
 1057 code Specific Contexts and Drive Context-Specific Fear Memory. *Neuron*. 2015; 87(6):1317–1331. doi:
 1058 [10.1016/j.neuron.2015.08.036](https://doi.org/10.1016/j.neuron.2015.08.036).
- 1059 Klaus A, Martins GJ, Paixao VB, Zhou P, Paninski L, Costa RM. The spatiotemporal organization of the striatum
 1060 encodes action space. *Neuron*. 2017; 95(5):1171.
- 1061 Lin X, Grieco SF, Jin S, Zhou P, Nie Q, Kwapis J, Wood MA, Baglietto-Vargas D, Laferla FM, Xu X. In vivo calcium
 1062 imaging of hippocampal neuronal network activity associated with memory behavior deficits in the Alzheimer's
 1063 disease mouse model. 2017 Neuroscience Meeting Planner Washinton, DC: Society for Neuroscience. 2017;
 1064 Poster.
- 1065 Mackevicius EM, Denisenko N, Fee MS. Neural sequences underlying the rapid learning of new syllables in
 1066 juvenile zebra finches. 2017 Neuroscience Meeting Planner Washinton, DC: Society for Neuroscience. 2017;
 1067 Poster.
- 1068 Madangopal R, Heins C, Caprioli D, Liang B, Barbera G, Komer L, Bossert J, Hope B, Shaham Y, Lin DT. In vivo calcium
 1069 imaging to assess the role of prelimbic cortex neuronal ensembles in encoding reinstatement of
 1070 palatable food-seeking in rats. 2017 Neuroscience Meeting Planner Washinton, DC: Society for Neuroscience.
 1071 2017; Poster.
- 1072 Markowitz JE, Liberti WA, Guitchounts G, Velho T, Lois C, Gardner TJ. Mesoscopic patterns of neural activity
 1073 support songbird cortical sequences. *PLoS biology*. 2015; 13(6):e1002158. doi: [10.1371/journal.pbio.1002158](https://doi.org/10.1371/journal.pbio.1002158).
- 1074 Mohammed AI, Gritton HJ, Tseng Ha, Bucklin ME, Yao Z, Han X. An integrative approach for analyzing hundreds
 1075 of neurons in task performing mice using wide-field calcium imaging. *Scientific reports*. 2016; 6.
- 1076 Mukamel EA, CellSort. Github; 2016. <https://github.com/mukamel-lab/CellSort>, 45f28d7.
- 1077 Mukamel EA, Nimmerjahn A, Schnitzer MJ. Automated Analysis of Cellular Signals from Large-Scale Calcium
 1078 Imaging Data. *Neuron*. 2009; 63(6):747–760. doi: [10.1016/j.neuron.2009.08.009](https://doi.org/10.1016/j.neuron.2009.08.009).
- 1079 Murugan M, Taliaferro JP, Park M, Jang H, Witten IB. Detecting action potentials in neuronal populations
 1080 with calcium imaging. 2016 Neuroscience Meeting Planner San Diego, CA: Society for Neuroscience. 2016;
 1081 Poster:260.11/GGG26.
- 1082 Murugan M, Park M, Taliaferro J, Jang HJ, Cox J, Parker N, Bhave V, Nectow A, Pillow J, Witten I. Combined social
 1083 and spatial coding in a descending projection from the prefrontal cortex. *bioRxiv*. 2017; p. 155929.
- 1084 Pachitariu M, Packer AM, Pettit N, Dalgleish H, Hausser M, Sahani M. Extracting regions of interest from
 1085 biological images with convolutional sparse block coding. In: *Advances in Neural Information Processing Systems*
 1086 26; 2013.p. 1745–1753.
- 1087 Pachitariu M, Stringer C, Schröder S, Dipoppa M, Rossi LF, Carandini M, Harris KD. Suite2p: beyond 10,000
 1088 neurons with standard two-photon microscopy. *bioRxiv*. 2016; p. 061507. doi: [10.1101/061507](https://doi.org/10.1101/061507).
- 1089 Pinto L, Dan Y. Cell-type-specific activity in prefrontal cortex during goal-directed behavior. *Neuron*. 2015;
 1090 87(2):437–451. doi: [10.1016/j.neuron.2015.06.021](https://doi.org/10.1016/j.neuron.2015.06.021).
- 1091 Pnevmatikakis EA, ca_source_extraction. Github; 2016. https://github.com/epnev/ca_source_extraction,
 1092 5a25d5a.

- 1093 **Pnevmatikakis EA**, Merel J, Pakman A, Paninski L. Bayesian spike inference from calcium imaging data. In: 1094 *2013 Asilomar Conference on Signals, Systems and Computers* IEEE; 2013. p. 349–353.
- 1095 **Pnevmatikakis EA**, Soudry D, Gao Y, Machado TA, Merel J, Pfau D, Reardon T, Mu Y, Lacefield C, Yang W, Ahrens 1096 M, Bruno R, Jessell TM, Peterka DS, Yuste R, Paninski L. Simultaneous denoising, deconvolution, and demixing 1097 of calcium imaging data. *Neuron*. 2016; 89(2):285–299.
- 1098 **Resendez SL**, Jennings JH, Ung RL, Namboodiri VMK, Zhou ZC, Otis JM, Nomura H, McHenry JA, Kosyk O, 1099 Stuber GD. Visualization of cortical, subcortical and deep brain neural circuit dynamics during naturalistic 1100 mammalian behavior with head-mounted microscopes and chronically implanted lenses. *Nature Protocols*. 1101 2016; 11(3):566–597. doi: [10.1038/nprot.2016.021](https://doi.org/10.1038/nprot.2016.021).
- 1102 **Roberts TF**, Hissey E, Tanaka M, Kearney MG, Chatterjee G, Yang CF, Shah NM, Mooney R. Identification of a 1103 motor-to-auditory pathway important for vocal learning. *Nature Neuroscience*. 2017; .
- 1104 **Rodriguez-Romaguera J**, Ung RL, Nomura H, Namboodiri VMK, Otis JM, Robinson JE, Resendez SL, McHenry JA, 1105 Eckman LEH, Kosyk TL, van den Munkhof HE, Zhou P, Paninski L, Kash TL, Bruchas MR, Stuber GD. Nociceptin 1106 neurons in the bed nucleus of the stria terminalis regulate anxiety. 2017 Neuroscience Meeting Planner 1107 Washinton, DC: Society for Neuroscience. 2017; Poster.
- 1108 **Rubin A**, Geva N, Sheintuch L, Ziv Y. Hippocampal ensemble dynamics timestamp events in long-term memory. 1109 *eLife*. 2015; 4(DECEMBER2015). doi: [10.7554/eLife.12247](https://doi.org/10.7554/eLife.12247).
- 1110 **Ryan PJ**, Ross SI, Campos CA, Derkach VA, Palmiter RD. Oxytocin-receptor-expressing neurons in the parabrachial 1111 nucleus regulate fluid intake. *Nature Neuroscience*. 2017; p. 1.
- 1112 **Sheintuch L**, Rubin A, Brande-Eilat N, Geva N, Sadeh N, Pinchasof O, Ziv Y. Tracking the Same Neurons across 1113 Multiple Days in Ca²⁺ Imaging Data. *Cell Reports*. 2017; 21(4):1102.
- 1114 **Smith SL**, Häusser M. Parallel processing of visual space by neighboring neurons in mouse visual cortex. *Nature 1115 neuroscience*. 2010; 13(9):1144–1149. doi: [10.1038/nn.2620](https://doi.org/10.1038/nn.2620).
- 1116 **Sun C**, Kitamura T, Yamamoto J, Martin J, Pignatelli M, Kitch LJ, Schnitzer MJ, Tonegawa S. Distinct speed 1117 dependence of entorhinal island and ocean cells, including respective grid cells. *Proceedings of the National 1118 Academy of Sciences*. 2015; 112(30):201511668. doi: [10.1073/pnas.1511668112](https://doi.org/10.1073/pnas.1511668112).
- 1119 **Tombaz T**, Dunn BA, Hovde K, R WJ. Action planning and action observation in rodent parietal cortex. 2016 1120 Neuroscience Meeting Planner San Diego, CA: Society for Neuroscience. 2016; Poster:247.06 / SS14.
- 1121 **Ung RL**, Rodriguez-Romaguera J, Nomura H, Namboodiri VMK, Otis JM, Robinson JE, Resendez SL, McHenry JA, 1122 Eckman LEH, Kosyk TL, van den Munkhof HE, Zhou P, Paninski L, Kash TL, Bruchas MR, Stuber GD. Encoding 1123 the relationship between anxiety-related behaviors and nociceptin neurons of the bed nucleus of the stria 1124 terminalis. 2017 Neuroscience Meeting Planner Washinton, DC: Society for Neuroscience. 2017; Poster.
- 1125 **Vogelstein JT**, Packer AM, Machado TA, Sippy T, Babadi B, Yuste R, Paninski L. Fast nonnegative deconvolution for 1126 spike train inference from population calcium imaging. *Journal of neurophysiology*. 2010; 104(6):3691–3704.
- 1127 **Vogelstein JT**, Watson BO, Packer AM, Yuste R, Jedynak B, Paninski L. Spike inference from calcium imaging 1128 using sequential Monte Carlo methods. *Biophysical journal*. 2009; 97(2):636–655.
- 1129 **Warp E**, Agarwal G, Wyart C, Friedmann D, Oldfield CS, Conner A, Del Bene F, Arrenberg AB, Baier H, Isacoff EY. 1130 Emergence of patterned activity in the developing zebrafish spinal cord. *Current Biology*. 2012; 22(2):93–102. 1131 doi: [10.1016/j.cub.2011.12.002](https://doi.org/10.1016/j.cub.2011.12.002).
- 1132 **Yu K**, Ahrens S, Zhang X, Schiff H, Ramakrishnan C, Fenno L, Deisseroth K, Zhao F, Luo MH, Gong L, He M, Zhou 1133 P, Paninski L, Li B. The central amygdala controls learning in the lateral amygdala. *Nature Neuroscience*. 2017; 1134 doi: [10.1038/s41593-017-0009-9](https://doi.org/10.1038/s41593-017-0009-9).
- 1135 **Zhou P**, CNMF-E. Github; 2017. https://github.com/zhoupc/CNMF_E, 088afc1.
- 1136 **Zhou P**, eLife_submission. Github; 2017. https://github.com/zhoupc/eLife_submission, 1c65f70.
- 1137 **Zhou P**, Resendez SL, Rodriguez-Romaguera J, Jimenez JC, Neufeld SQ, Giovannucci A, Friedrich J, Pnevmatikakis 1138 EE, Stuber GD, Hen R, Kheirbek MA, Sabatini BL, Kass RE, Paninski L, Data from: Efficient and accurate 1139 extraction of in vivo calcium signals from microendoscopic video data. Dryad Digital Repository; 2017. 1140 doi: <https://doi.org/10.5061/dryad.kr17k>, doi: [doi:10.5061/dryad.kr17k](https://doi.org/10.5061/dryad.kr17k).

- 1141 Ziv Y, Burns LD, Cocker ED, Hamel EO, Ghosh KK, Kitch LJ, El Gamal A, Schnitzer MJ. Long-term dynamics of CA1
1142 hippocampal place codes. *Nature neuroscience*. 2013; 16(3):264–6. doi: [10.1038/nn.3329](https://doi.org/10.1038/nn.3329).
- 1143 Ziv Y, Ghosh KK. Miniature microscopes for large-scale imaging of neuronal activity in freely behaving rodents.
1144 *Current Opinion in Neurobiology*. 2015; 32:141–147. doi: [10.1016/j.conb.2015.04.001](https://doi.org/10.1016/j.conb.2015.04.001).